PLANETESIMAL ACCRETION AT SHORT ORBITAL PERIODS

Spencer C. Wallace[1] and Thomas R. Quinn[1]

[1]Astronomy Department, University of Washington, Seattle, WA 98195

ABSTRACT

Formation models in which terrestrial bodies grow via the pairwise accretion of planetesimals have been reasonably successful at reproducing the general properties of the solar system, including small body populations. However, planetesimal accretion has not yet been fully explored in the context of the **wide variety** of recently discovered extrasolar planetary systems, particularly those that host short-period terrestrial planets. In this work, we use direct N-body simulations to explore and understand the growth of planetary embryos from planetesimals in disks extending down to $\simeq 1$ day orbital periods. We show that planetesimal accretion becomes nearly 100 percent efficient at short orbital periods, leading to embryo masses that are much larger than the classical isolation mass. For rocky bodies, the physical size of the object begins to occupy a significant fraction of its Hill sphere towards the inner edge of the disk. In this regime, most close encounters result in collisions, rather than scattering, and the system does not develop a bimodal population **of** dynamically hot planetesimals and dynamically cold oligarchs, like is seen in previous studies. The highly efficient accretion seen at short orbital periods implies that systems of tightly-packed inner planets should be almost completely devoid of any residual small bodies. We demonstrate the robustness of our results to assumptions about the initial disk model, and also investigate **the effects** that our simplified collision model has on the emergence of this non-oligarchic growth mode in a planet forming disk.

1. INTRODUCTION

Planetesimal accretion is a key phase in the terrestrial planet growth process, bridging the gap from kilometer-sized bodies up to roughly moon-sized objects known as planetary embryos. In the earliest stages of the planet formation process, **beginning from μm sizes,** aerodynamic forces dominate the growth and evolution of the solids and statistical models (Johansen et al. 2014; Birnstiel et al. 2016) are appropriate to describe how these numerous, small bodies coagulate.

Due to the internal pressure support of the gas disk, the gas itself orbits at sub-Keplerian speed and exerts a headwind on any solids large enough to decouple from the gas (Weidenschilling 1977). Around a meter in size, this headwind is maximally effective at sapping away orbital angular momentum, and planet-building material can fall onto the central star on catastrophically short timescales (Weidenschilling 1977; Nakagawa et al. 1986). Additionally, laboratory experiments suggest that collisions between mm- to cm- sized solids tend to result in bounces or destruction, rather than continued growth (Blum & Münch 1993; Colwell 2003; Beitz et al. 2011).

For these reasons, a number of mechanisms to radially concentrate solids in a planet-forming disk have been proposed to facilitate fast growth from mm to km sizes (Johansen et al. 2007; Lyra et al. 2008; Bai & Stone 2010) in order to surmount these barriers. Interestingly, formation models for the short-period multiplanet systems revealed by Kepler (Fabrycky et al. 2014) also seem to require enhanced concentrations of planet-building material to reproduce the observed architectures (Raymond et al. 2007; Hansen & Murray 2012).

Regardless of how the mm- to km-sized growth barriers are surmounted, gravity begins to dominate and aerodynamic gas drag plays an increasingly unimportant role beyond this size. During this phase, collision cross sections are enhanced as gravitational focusing (Safronov 1969) acts to bend the trajectories of bodies undergoing close encounters. Because gravitational focusing becomes more effective as bodies grow larger, a period of runaway growth occurs (Wetherill & Stewart 1989; Kokubo & Ida 1996; Barnes et al. 2009) and a power law spectrum of masses develop. Eventually, the largest bodies (known as oligarchs) dynamically heat the remaining planetesimals, severely limiting further growth (Kokubo & Ida 1998). The final outcome of this phase is a bimodal population of dynamically cold oligarchs, surrounded by dynamically hot, difficult to accrete residual planetesimals. Lines of evidence suggest that the asteroid belt (**Bottke et al. 2005; Morbidelli et al. 2009**), Kuiper belt (**Duncan et al. 1989; Levison et al. 2008; Sheppard & Trujillo 2010**) and the

Oort cloud (Levison et al. 2011) are largely composed of the leftovers of this stage of planet formation.

Tidal interactions between protoplanets and the gaseous disk keep eccentricities and inclinations low until the gas disk dissipates (typically over the course of a few Myr (Mamajek 2009)). Eventually, gravitational perturbations eventually trigger an instability which drives bodies onto crossing orbits. This instability occurs on a timescale of $\sim 10^5$ years and involves large scale oscillations of the eccentricity and inclinations of the bodies as they strongly interact through secular resonances (Chambers & Wetherill 1998). As a consequence of the instability, the oligarchics are no longer on isolated, stable orbits and coalesce to form Earth-sized planets through a series of extremely energetic giant impacts (Kokubo & Ida 2002; Raymond et al. 2005, 2006).

Due to the relative ease of modeling the early dust coagulation phases and the final giant impact phase, these steps in the terrestrial planet formation process have received most of the attention in the literature. The planetesimal accretion phase, which we will focus on in this paper, is more difficult and expensive to model because there are too many particles to directly track with traditional N-body codes, while the gravitational interactions between the **few massive bodies produced by the runaway growth phase (Ida & Makino 1993; Kokubo & Ida 1995, 1998) render statistical methods inappropriate**. Due to computational expense, N-body simulations of planetesimal accretion are usually modeled in a narrow ring (Kokubo & Ida 1996, 1998), and the results and timescales are then scaled to suit whatever relevant orbital period is being studied. N-body simulations of terrestrial planet assembly typically begin with a series of neatly spaced oligarchs, whose mass varies smoothly with orbital period. As we will show in this paper, oligarchic growth does not scale to arbitrarily short orbital periods.

Given that Systems of Tightly-packed Inner Planets (STIPs) appear to be a common outcome of planet formation (Latham et al. 2011; Lissauer et al. 2011; Rowe et al. 2014), understanding exactly how solids accumulate at short orbital periods is crucial. Although gasdisk driven migration of the planets themselves is often invoked to explain the observed architectures (Izidoro et al. 2017, 2021), we will focus on an in-situ model in this paper. That is, once the planetesimals themselves form, they largely stay in place, and any subsequent large-scale movement of the solids are the result of mutual gravitational interactions. The focus of this work will be to understand how the outcome of the planetesimal accretion process scales with orbital period by using a high-powered N-body code to directly follow the growth and evolution of the planetesimals across a wide range of orbital periods (1 to 100 days). In doing so, we will assess whether the typical initial conditions (fully formed, evenly spaced protoplanets, e.g. Raymond et al. (2006)) used in studies of terrestrial planet formation are actually appropriate for understanding STIPs.

In section 2 we provide an overview of the theory behind planetesimal accretion and show that assumptions used to derive the well-known modes of growth are only valid at sufficiently long orbital periods. We then motivate the need for N-body simulations to study this problem and describe the code used, along with how our initial conditions were constructed in section 3. In section 4, we present a parameter study of planetesimal accretion using a series of simulations of narrow annuli that exhibit both oligarchic and non-oligarchic growth. In section 5 we present a set of simulations starting with a wide planetesimal disk and demonstrate that a transition between accretion modes occurs at moderately small orbital periods. Next, we assess the impact of simplifications made to our collision model on this result in section 6. In section 7, we discuss the implications of this multimodal accretion behavior throughout the disk for planet formation models and conclude.

2. OVERVIEW OF PLANETESIMAL ACCRETION

2.1. *Oligarchic and Runaway Growth*

We begin our analysis by considering a disk of equal mass planetesimals with radius r_{pl}, mass m_{pl} and surface density Σ_{pl}. The collision rate in the vicinity of an orbit defined by Keplerian frequency Ω can be written as $n\Gamma v$, where $n = \Sigma_{pl}\Omega/2m_{pl}v$ (where we have assumed that the scale height of the planetesimal disk goes as $2v/\Omega$). Γ describes the effective collision cross section and v is the typical encounter velocity between planetesimals. For a swarm of planetesimals on randomly oriented orbits, v is typically taken to the rms velocity $\langle v^2 \rangle^{1/2}$, which can be related to the eccentricity and inclination distribution (e, i) in the following way (Lissauer & Stewart 1993):

$$\langle v^2 \rangle^{1/2} = \left(\frac{5}{4} \langle e^2 \rangle^{1/2} + \langle i^2 \rangle^{1/2} \right) v_k. \qquad (1)$$

The dynamical interactions between growing planetesimals can be somewhat simplified by scaling the orbital elements of the bodies by the Hill radius

$$r_h = \left(\frac{m_{pl}}{3M_*} \right)^{1/3}, \qquad (2)$$

where M_* is the mass of the central star. The **Hill radius of a body gives distance where the gravity of the growing planetesimal dominates over the gravity of the star. Using equation 2, the eccentricity, inclination and separation between orbiting bodies can be defined as**

$$e_h = \frac{ae}{r_h}, \; i_h = \frac{ai}{r_h}, \; \tilde{b} = \frac{a_2 - a_1}{r_h}. \tag{3}$$

Using this formalism, e_h and i_h describe the radial and vertical excursions of an orbiting body in units of its Hill radius. For $e_h > 1$, the random velocity dispersion dominates over the shearing motion over a separation of $1 r_h$ and encounters can be treated with a two-body formalism.

Assuming that every collision results in a perfect merger, the growth rate of a planetesimal is given by

$$\frac{1}{M}\frac{dM}{dt} = \frac{\Sigma \Omega}{2 m_{pl}} \Gamma. \tag{4}$$

In the case where the collision cross section depends only on the physical size of the planetesimals, the growth scales sub-linearly with mass and the mass distribution is expected to evolve in an "orderly" fashion, in which mass ratios between bodies tend toward unity. However, bodies larger than ~ 100 km in size are expected to exert a significant gravitational force on each other during encounters and the collision cross section depends on both the size of the bodies and their encounter velocities. In this case,

$$\Gamma = \pi r_{pl}^2 \left(1 + v_{esc}^2/v^2 \right) \tag{5}$$

(Safronov 1969), where v_{esc} is the escape velocity from the two bodies at the point of contact.

In the limit that $v_{esc} \gg v$, it can be shown that $dM/dt \propto M^{4/3}$, which implies a runaway scenario where growth accelerates with mass. This mode of growth was confirmed with N-body simulations by Kokubo & Ida (1996) and appears necessary to construct protoplanets within the lifetime of a protoplanetary disk (**Lissauer 1987), although one should note that pebble accretion (Lambrechts & Johansen 2012, 2014; Bitsch et al. 2015) is a viable alternative scenario**. Due to the velocity dependence of the gravitational focusing effect, it is not clear how ubiquitous this mode of growth is. In particular, encounter velocities at short orbital periods will be rather large (because $v \sim v_k$) and the $v_{esc} \gg v$ condition may not always be satisfied. The effect that a dynamically hot disk has on runway growth will be examined in detail in section 4.

An important feature is missing from the model described above, which limits its applicability at late times. Gravitational stirring, which converts Keplerian shear into random motion, raises the typical encounter velocity between planetesimals over time (Weidenschilling 1989; Ida 1990) and diminishes the effectiveness of gravitational focusing. As the mass spectrum of the system evolves away from uniformity, these velocity differences become even more pronounced. As the system evolves, it tends toward a state of energy equipartition where $v \sim m^{1/2}$. For a system of equal mass bodies in which encounters are driven by random motions rather than Keplerian shear (dispersion dominated), the timescale for gravitational stirring is described by the two-body relaxation time (Ida & Makino 1993)

$$t_{relax} = \frac{v^3}{4 \pi n G^2 m_{pl}^2 \ln \Lambda}, \tag{6}$$

where $\ln \Lambda$ is the Coulomb logarithm, typically taken to be ≈ 3 **for a planetesimal disk (Ida 1990; Stewart & Ida 2000)**. Despite the fact that the behavior of gravitational stirring is well-described by a two-body formula, (Ida & Makino 1993) found that the stirring in a planetesimal disk is actually driven by close encounters, which requires a three-body formalism. As we will show in section 4, gravitational stirring effectively shuts off when the Hill sphere of a body becomes comparable to its physical size. In this case, close encounters tend to result in collisions, and the main pathway for energy exchange between planetesimals and growing protoplanets is unable to operate.

Kokubo & Ida (1998) showed that **the runaway growth process described above** is actually self-limiting. As the runaway bodies develop, they become increasingly effective at **dynamically** heating the remaining planetesimals, which diminishes the gravitational focusing cross sections and throttles the growth rate. Around the time that the mass of the runaway bodies exceeds the mass of the planetesimals by a factor of $\sim 50 - 100$ (Ida & Makino 1993) a phase of less vigorous "oligarchic" growth commences, in which the largest bodies continue to accrete planetesimals at similar rates, independent of mass.

Regardless of the mechanism that eventually limits the growth of the planetary embryos, a maximum estimate for the masses produced during this stage of accretion can be obtained using the initial solid surface density profile. A growing protoplanet will eventually accrete material within a distance $b = \tilde{b} r_h$ of its orbit. The total mass of planetesimals within this feeding zone is then $2\pi a \left(2\tilde{b} r_h \right) \Sigma_{pl}$, where a is the semimajor axis of the growing protoplanet and Σ_{pl} is the initial local planetesimal surface density. The "'isola-

tion mass" of the protoplanet can then be obtained by setting the protoplanet mass equal to the total mass of planetesimals within the feeding zone such that

$$M_{iso} = 4\pi a^2 \tilde{b} \left(\frac{M_{iso}}{3M_*}\right)^{1/3} \Sigma_{pl}. \tag{7}$$

Solving for M_{iso} gives

$$M_{iso} = \left[\frac{\left(2\pi a^2 \Sigma_{pl} \tilde{b}\right)^3}{3M_*}\right]^{1/2}. \tag{8}$$

For bodies on circular, non-inclined orbits, $\tilde{b} = 2\sqrt{3}$ is the smallest orbital separation that produces a non-negative Jacobi energy and permits a close encounter (Nakazawa & Ida 1988). This value of $\tilde{b}$ is typically used to calculate the final isolation mass of a protoplanet, as oligarchic growth tends to ensure that embryos stay on near-circular orbits as they grow.

The picture described above relies upon **a** crucial assumption, which is that the mass distribution evolves slowly enough for gravitational stirring to maintain energy equipartition. In other words, the relaxation timescale must remain short relative to the **collision** timescale. For typical conditions near the terrestrial region of the solar system, this timescale condition is satisfied. Due to the steep dependence of the relaxation time on encounter velocity, however, this condition can easily be violated at shorter orbital periods.

In figure 1, we show the ratio between the relaxation and collision timescale for a population of equal-mass planetesimals as a function of orbital period. Here, the encounter velocity is described by equation 1. For simplicity, we assume that $\left\langle e^2\right\rangle^{1/2} = 2\left\langle i^2\right\rangle^{1/2}$ (Ida et al. 1993) and that the eccentricity dispersion is constant with orbital period. **The coloring indicates the ratio between t_{relax} and t_{coll}. The dashed lines denote the eccentricity at which the random encounter velocity (calculated according to equation 1) is equal to the mutual escape velocity of the bodies. This is shown for planetesimals with an internal density of 3 g cm^{-3} ranging from 10 to 200 km in size.**

A physically realistic value of e_h for a population of planetesimals is going to depend on the structure of the gaseous disk (which we will address in section 5). However, the eccentricity dispersion will typically increase over time until $\left\langle v^2\right\rangle^{1/2} = v_{esc}$ and this is often used to construct the initial conditions (e.g. Barnes et al. (2009)).
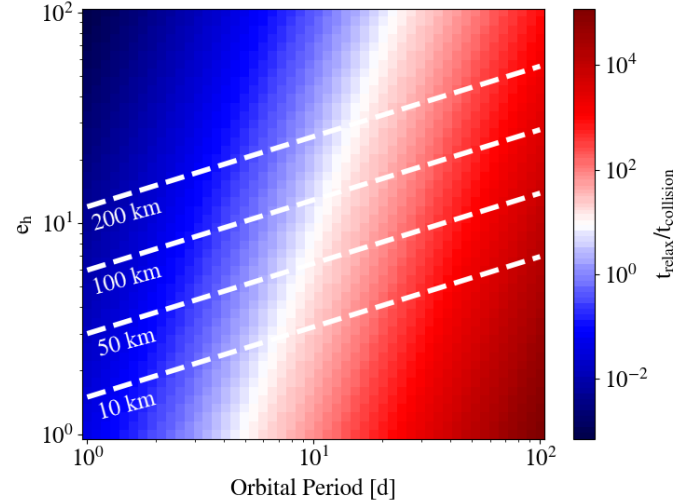

Figure 1. The ratio between the two-body relaxation and collision timescale for a population of equal-mass planetesimals with an internal density of 3 g cm^{-3}. **The dashed curves show the value of e_h for which the random velocity dispersion is equal to the escape velocity of the planetesimals for a range of sizes.** Only in regions where $t_{relax} \gg t_{coll}$ can the velocity distribution respond to changes in the mass of the bodies such that oligarchic growth can operate. This condition is no longer satisfied for a dynamically hot disk at sufficiently short orbital periods.

Therefore, the curves in this figure should be interpreted as upper limits.

The timescale criterion for oligarchic growth is only satisfied in regions where the disk is sufficiently dynamically cold and the orbital period is sufficiently long. In sections 4 and 5 we will explore the behavior and outcome of planetesimal accretion in regions where this criterion is *not* satisfied.

2.2. *Planetesimal Size and Extent of Hill Sphere*

In the formalism described above, the mass and velocity distribution of the bodies are both a function of time. Due to the interdependence of these quantities, it is not clear whether the **ratio between the relaxation and collision timescales will remain constant** as the oligarchs develop. In the case of the solar system, $t_{relax} \ll t_{coll}$ likely continued to remain true, otherwise runaway growth would have consumed all of the small bodies and there would be nothing left to populate the asteroid or Kuiper belt. In the case where $t_{coll} \ll t_{relax}$, however, it is not clear how the system might evolve.

An insight into the expected behavior in this regime can be gained by defining a dimensionless parameter, α, which is the ratio between the physical size of a body

and its Hill radius, r_h

$$\alpha = \frac{r_{pl}}{r_h} = \frac{1}{a}\left(\frac{9M_\star}{4\pi\rho_{pl}}\right)^{1/3}, \qquad (9)$$

where a is the semimajor axis of the body and ρ_{pl} is its bulk density. Assuming that the bulk density stays constant as bodies collide and grow, and that no large-scale migration occurs, the scaling of both r_{pl} and r_h as $m_{pl}^{1/3}$ means that α will be constant with time. For a composition of ice and rock, α is small for any presently populated region of the solar system ($\alpha \sim 10^{-2}$ near Earth and $\alpha \sim 10^{-4}$ in the Kuiper belt). As one moves closer to the sun, α becomes larger than 1, which implies that the Hill sphere of a body becomes smaller than its physical size. **As an additional note, the Roche limit of the central body and the distance at which $\alpha = 1$ are similar, but not identical. For a rigid spherical body, $a_{Roche} \simeq 0.88 a_{\alpha=1}$. Applying a hydrostatic correction to the Roche limit, $a_{Roche} \simeq 0.6 a_{\alpha=1}$. This accretion mode should therefore be relevant for ring systems.**

The magnitude of α controls the relative importance of gravitational scattering and collisions in driving the evolution of the planetesimal disk. When α is small, most close encounters will result in a gravitational interaction, moving the system toward a state of relaxation. If, however, the Hill sphere is largely filled by the body itself, these same encounters will instead drive evolution of the mass spectrum. Because α stays constant with mass, the boundary in the disk where collisions or gravitational encounters dominate, will stay static with time.

We also introduce a second dimensionless quantity, which relates the physical size of the bodies to the velocity state of the system

$$\beta = \frac{r_{pl}}{r_g}. \qquad (10)$$

where $r_g = Gm_{pl}/v^2$ is the gravitational radius of a body (see eq 4.1 of Ida (1990)). Encounters between bodies inside of a distance of r_g result in significant deflections of their trajectories. It should be noted that the gravitational focusing enhancement factor v^2/v_{esc}^2 is equal to 1 for $\beta = 1$. In the case where r_g is smaller than the size of a planetesimal, the gravitational focusing enhancement factor will be between 0 and 1 and the collision cross section is mostly set by the geometric value. **For very large values of r_g ($\beta \gg 1$), the effective collision cross section is almost entirely set by gravitational scattering.**

These scaling considerations motivate the range of parameters we choose for the numerical experiments presented in the next section, where we aim to understand where and when runaway and oligarchic growth can operate.

3. NUMERICAL METHODS

We use the tree-based N-body code CHaNGa[1] to model the gravitational and collisional evolution of a swarm of planetesimals. CHaNGa is written using the CHARM++ parallel programming language and has been shown to perform well on up to half a million processors (Menon et al. 2015) and can follow the evolution of gravitationally interacting collections of up to billions of particles. Using a modified Barnes-Hut tree with hexadecapole expansions of the moments to approximate forces, CHaNGa integrates the equations of motion using a kick-drift-kick leapfrog scheme. For all of the simulations presented in this paper, we use a node opening criteria of $\theta_{BH} = 0.7$. Additional information about the code is available in (Jetley et al. 2008; Menon et al. 2015).

Using the neighbor-finding algorithm in CHaNGa, originally designed for SPH calculations, we have recently implemented a solid body collision module in the code. This work is largely based on the solid-body collision implementation in PKDGRAV, which is described in Richardson (1994) and Richardson et al. (2000). To summarize, imminent collisions are detected during the "drift" phase by extrapolating positions of bodies forward in time, using the velocity calculated at the opening "kick". For each body, any neighboring particles which fall within a search ball of radius $2\Delta Tv + 2r_{pl}$, where ΔT is the current timestep size for the particle and v is magnitude of its heliocentric velocity, are tested for an imminent collision. In the case that a collision is detected, the particles are merged into a single larger body, which is given the center of mass position and velocity of the two **parents**. Resolving a collision can produce another imminent collision, so collisions are handled one-by-one and another full collision check is run after the previous event is resolved. For a more detailed description of the collision module in CHaNGa, see (Wallace & Quinn 2019). Particles are advanced on individual timesteps chosen as a power of two of a base timestep. The timestep for an individual particle is based on an estimate of the gravitational dynamical time determined by the minimum of $\sqrt{d_{node}^3/(G(M_{node} + m_{pl}))}$ across all nodes in the tree that are accepted by the Barnes-Hut opening criterion. Here d_{node} is the distance from the planetesimal to the center of mass of the tree node and M_{node} is the total

---

[1] A public version of CHaNGa can be downloaded from http://www-hpcc.astro.washington.edu/tools/ChaNGa.html
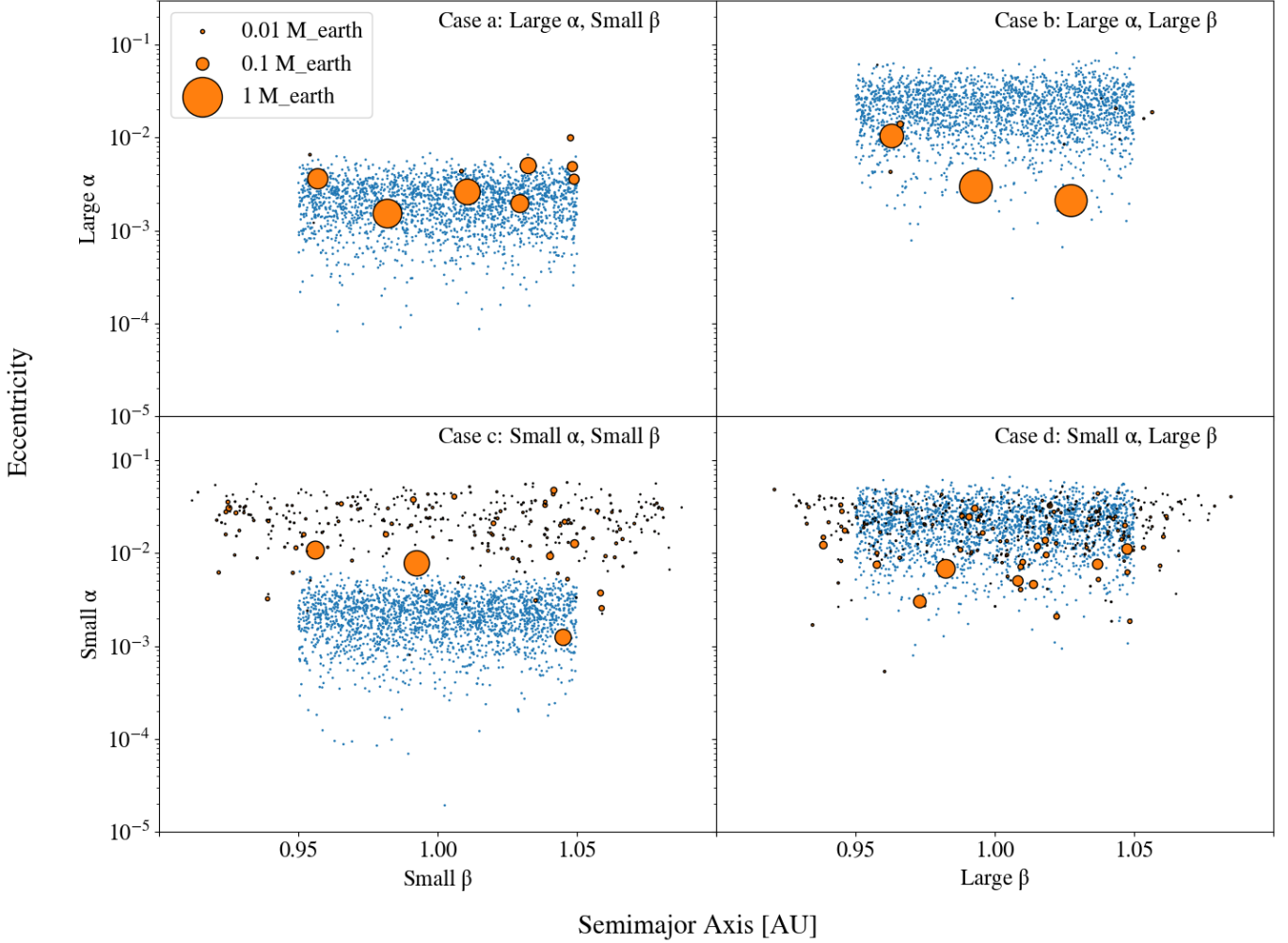
Figure 2. The initial (blue) and final (orange) states of the narrow annulus simulations described in section 4. Relative masses of the bodies are indicated by point size. In the case of large α, almost no residual planetesimal population remains. Regardless of the initial choice of β, the protoplanets that form attain similar eccentricities.

mass of the tree node. For nearby particles M_{node} is replaced with the mass of the nearby particle.

4. NARROW ANNULUS SIMULATIONS

We begin by **exploring the outcome of planetesimal accretion in different parts of the (α, β) parameter space.** The choices of α and β are motivated by two questions raised in section 2. 1) Does runaway growth still operate when the condition that $v \ll v_{esc}$ is not satisfied? 2) How does planetesimal accretion proceed when the planetesimals themselves occupy a significant fraction of their Hill spheres?

To answer these questions, we run a series of simulations in which a narrow annulus of planetesimals orbits a star. The values of α and β are varied individually. 4000 planetesimals with individual masses of $8.37 \times 10^{-5} M_{\oplus}$ are placed with semimajor axes drawn **from a uniform distribution** between 0.95 and 1.05 AU about a 1 $M_{\odot}$ star. **In total, the disk contains ~ 0.33 $M_{\oplus}$ of material.** The argument of perihelion, ω, longitude of ascending node, Ω, and mean anomaly, M, for each body is drawn from a uniform distribution $\in [0, 2\pi)$. The inclinations and eccentricities are drawn from a Rayleigh distribution with $\langle i^2 \rangle = 1/2 \langle e^2 \rangle$ (Ida et al. 1993).

In the "fiducial" case, we give the bodies a bulk density of 3 g cm^{-3} **(for a radius of 341 km)**, and $\langle e^2 \rangle^{1/2} = 4e_h$, which corresponds to $\alpha = 3.6 \times 10^{-2}$ and $\beta = 3.4 \times 10^{-3}$. These parameters are chosen to match the initial conditions of Kokubo & Ida (1998), which gave rise to oligarchic growth. To vary the value of α, we alter the bulk density of the particles. In the high-α case, the bulk density is reduced by a factor of ~ 7100, which produces $\alpha = 1$. **This corresponds to a bulk density of 4.2×10^{-4} g cm^{-3} and a radius of 6,500 km. Although this is most certainly**
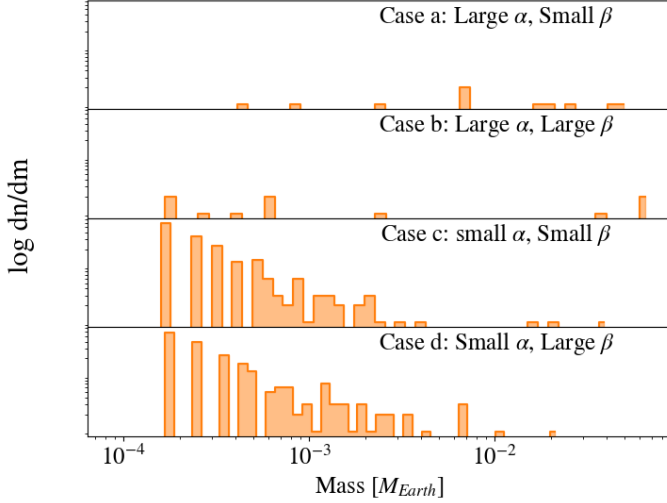
Figure 3. The final state of the mass distributions for the narrow annulus simulations described in section 4. For small α, a few embryos form alongside a power law tail of planetesimals. For larger values of α, the mass distribution stops being bimodal. As in the previous figure, the initial choice of β does not appear to have any meaningful impact on the end result.
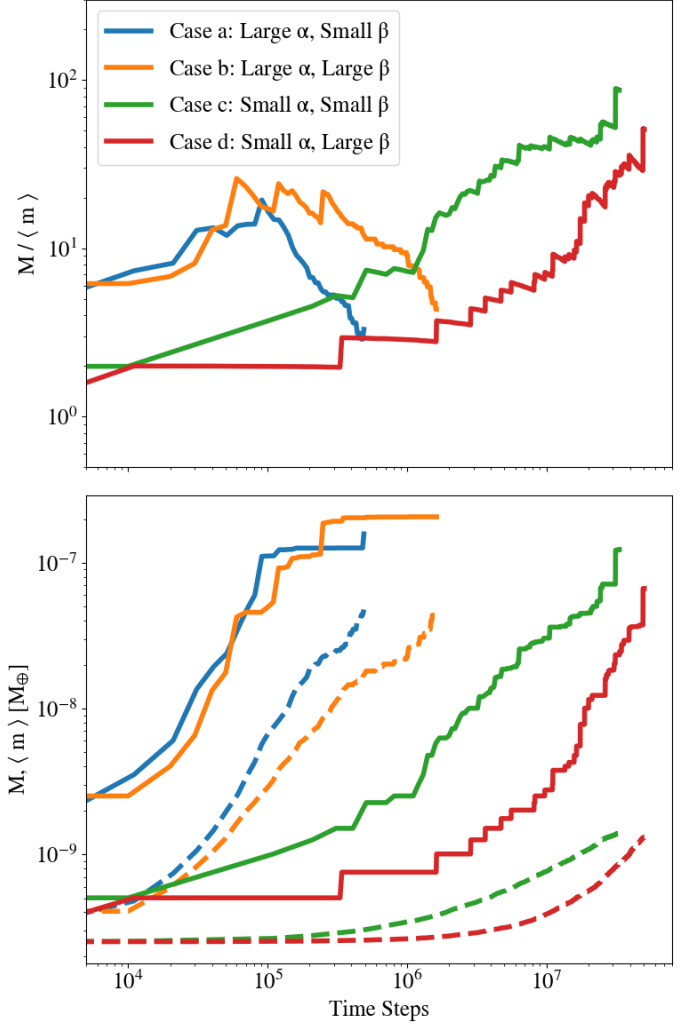

Figure 4. Top: The evolution of the ratio between the maximum and mean mass for the four simulations presented in section 4. The runaway growth phase can be identified by a positive trend in this ratio. For all values of α, an increase in β has the effect of delaying runaway growth. **Bottom: The evolution of the maximum (solid lines) and mean (dashed lines) shown individually.**

458 **unphysical, the purpose of this modification is**
459 **to have a planetesimal completely fills its Hill**
460 **sphere so that no strong gravitational scattering**
461 **should occur.** To vary β, the eccentricity dispersion
462 is increased. For the high-β case, $\langle e^2 \rangle^{1/2}$ is increased
463 to $1500 e_h$, which corresponds to $\beta = 15,000$. **This is**
464 **the largest value of β that permits a particle at**
465 **1 AU to still have an apocenter and pericenter**
466 **distance that lies within the boundaries of the**
467 **disk. This choice of β places the system firmly**
468 **in the $v > v_{esc}$ regime, while still allowing growth**
469 **to occur in a reasonable number of timesteps.**
470 In all cases, the simulations are evolved with a base
471 timestep of 1.7 days, which corresponds to 3% of an
472 orbital dynamical time $\sqrt{a^3/GM_*}$. Due to the vastly
473 differing growth timescales in each case, a simulation
474 is stopped when the growth of the most massive body
475 flattens out. In figure 2, we show the a-e distribution
476 of bodies in the initial (blue) and final (orange) snap-
477 shots from each of the 4 simulations. The size of the
478 points indicates the relative masses of the bodies. Only
479 **with small α (case c, d)** does a residual population
480 of dynamically hot planetesimals develop. The lack of
481 high eccentricity planetesimals **(relative to the pro-**
482 **toplanets)** in the large α **(case a, b) simulations**
483 suggests that most encounters result in accretion rather
484 than scattering. **For** large β **(case b, d)**, the **growing**
485 protoplanets and end up in a dynamically cool state,

486 **relative** with the initial conditions. This is due to ki-
487 netic energy being lost as particles inelastically collide.
488 One last point we note is the difference between the ec-
489 centricities of protoplanets in the large α, large β **(case**
490 **b)** and the small α, large β **(case d) simulation**. The
491 dynamically cooler result of the **former** case is likely
492 due to the dominant role that inelastic collisions play
493 here.
494 In figure 3, we show the mass distribution of bod-
495 ies from the final snapshot in each of the four **simula-**
496 **tions**. In addition to leaving fewer residual planetesi-
497 mals, the large α **(case a, b)** simulations produce **em-**

bryos that are a factor of a few larger. Despite the vastly different encounter velocities of each population of bodies, the initial size of β (so long as bodies remain in the dispersion-dominated regime) appears to have no significant effect on the final distribution of masses. **For reference, the boundary between shear and dispersion-dominated encounters (e_h = 1) lies around e = 4×10^{-4} for the planetesimal mass we have chosen. The eccentricity at which $\langle v^2 \rangle^{1/2} = v_{esc}$ for the planetesimals is around 10^{-2}.** To investigate whether any of these planetesimal rings underwent runaway growth, we examine the time evolution of the maximum and mean masses in each simulation. The ratio $M/\langle m \rangle$ is plotted in **the top panel of** figure 4. **Here**, a positive slope indicates that the quantities are diverging (i.e. the growth rate is accelerating with mass). This behavior is evident in all four cases **although the small α simulations eventually reach a stage where the curves turn over as the planetesimal supply depletes.**. Even with a large β, where the effective collision cross section is nearly equal to the geometric value, runaway growth still appears to operate. The ubiquity of the early positive trends in this figure suggests that as bodies collide and grow, the relative difference in gravitational focusing factors between bodies is what drives the system towards runaway growth, no matter how close the collision cross sections lie to the geometric value. Although larger encounter velocities lengthen the growth timescales, runaway growth appears to be inevitable, so long as gravity is the dominant force in the system. For large α **(case a, b)**, the curves in this figure eventually turn over and begin to decline. **In the bottom panel of figure 4, we separately show the evolution of the maximum (solid lines) and mean (dashed lines) mass for each case. Here, it is evident that the turnover in $M/\langle m \rangle$ is driven by an increase in the average mass as the planetesimal population becomes depleted. For small α, one would expect that planetesimal accretion should also eventually come to a halt as the growth timescale lengthens due to the planetesimal surface density decreasing and the residual bodies being scattered onto high eccentricity orbits with negligible gravitational focusing factors. Many more timesteps, however, would be required to reach this point.**

Additionally, these results suggest that the value of α, which is a function of only the initial conditions, controls the qualitative outcome of accretion. Across most of a planet-forming disk, α is small, and frequent gravitational encounters between the growing bodies will facilitate oligarchic growth. In the dispersion-dominated regime, close encounters drive the stirring between planetesimals and embryos (Weidenschilling 1989; Ida 1990). **When $\alpha \ll 1$, the Hill sphere of a body is mostly empty space and the majority of close encounters result in viscous stirring, rather than accretion. In the opposite regime,** we observe that runaway growth still occurs, but nearly all of the planetesimals are consumed by the forming protoplanets, rather than being scattered onto higher eccentricity orbits, where they would otherwise remain as a remnant of the early stages of planet formation (Kokubo & Ida 1998, 2000).

5. FULL DISK SIMULATION

5.1. *Initial Conditions*

Motivated by the qualitative dependence of accretion on α, we next investigate whether this highly efficient, non-oligarchic growth should be expected to operate near the innermost regions of a typical planet-forming disk. Given that N-body simulations of short-period terrestrial planet formation typically begin with a chain of neatly-spaced, isolation mass (see Kokubo & Ida (2000) eq. 20) protoplanets, it is pertinent to determine whether the high α growth mode we revealed in the previous section invalidates this choice of initial conditions.

Given the dearth of short-period terrestrial planets observed around M stars (e.g. TRAPPIST-1 (Gillon et al. 2016, 2017; Agol et al. 2021)), we chose to model the evolution of a series of wide planetesimal disks, which span from 1 to 100 days in orbital period, orbiting a late-type M star of mass 0.08 $M_\odot$. For a population of planetesimals with a bulk density of 3 g cm^{-3}, this orbital period range corresponds to $\alpha \in (0.7, 0.05)$. By simultaneously modeling a broad range of orbital periods, we can determine the critical value of α that divides these two modes of accretion, and also explore how the oligarchic/non-oligarchic accretion boundary affects the resulting distribution of protoplanets.

Four wide-disk simulations are run in total (see table 1). In each case, the solid surface density follows a power law profile

$$\Sigma(r) = 10 \text{ g cm}^{-2} \times A \left(\frac{M_*}{M_\odot} \right) \left(\frac{r}{1 \text{ AU}} \right)^{-\delta} \qquad (11)$$

where M_* is the mass of the central star, $\Sigma_{MMSN} = 10$ g cm^{-2} is the surface density of the minimum-mass solar nebula (Hayashi 1981) at 1 AU, A is an enhancement factor and δ is the power law index. In the first case (fdHi), we model a disk that follows a MMSN power law slope ($\delta = 1.5$), with the overall normalization enhanced by a factor of 100. This choice of normalization for the solid surface density profile appears nec-

essary in order to reproduce many observed short period terrestrial worlds in-situ (Hansen & Murray 2012). **The most current planetesimal formation models all involve streaming instabilities triggered by solid material concentrating at preferential locations in the disk. This can occur via zonal flows** (Johansen et al. 2009; Simon et al. 2012), **vortices** (Klahr & Bodenheimer 2003), **or through mechanisms that produce a pressure bump in the gas disk, such as an ionization** (Lyra et al. 2008) **or condensation front** (Brauer et al. 2008; Drkażkowska et al. 2013), **or even the perturbations from an existing planet** (Shibaike & Alibert 2020). Drkażkowska & Dullemond (2018) **showed that evolution of the snow line boundary can cause planetesimal formation over a significant area of the disk, producing mass concentrations at least as large as the ones we use here. We argue that this is a particularly attractive mechanism for widespread planetesimal formation around low-mass stars, as their extreme pre-main sequence evolution is particularly conducive to significant movement of the condensation fronts** (Baraffe et al. 2015).

Additionally, we vary the power law index (fdHiShallow, fdHiSteep) and overall normalization (fdLo) of $\Sigma(r)$. **Although there is no way to reliably measure the uncertainty on the MMSN power law slope,** Chiang & Laughlin (2013) **applied a similar analysis to a sample of Kepler multiplanet systems and found a variation of ~ 0.2. Submillimeter observations of the outer regions of cold protoplanetary disks find that δ can be as low as 0.5** (Mundy et al. 2000; Andrews et al. 2009, 2010). **Therefore, we vary δ by a value of 1.0 relative to the MMSN value for the fdHiShallow and fdHiSteep simulations.**

In all cases, the eccentricities and inclinations of the bodies are randomly drawn from a Rayleigh distribution, with $\left\langle e^2 \right\rangle^{1/2} = 2\left\langle i^2 \right\rangle^{1/2} = e_{eq}$ (Ida & Makino 1993). **Following** Kokubo & Ida (1998), **the value of e_{eq} is chosen such that the timescales for viscous stirring and aerodynamic gas drag on the planetesimals are in equilibrium. Although this approach assumes that these two mechanisms are in balance, there is nothing preventing planetesimal accretion from getting underway before the disk is sufficiently hot to be limited by gas drag. However, as we showed in the previous section, the initial dynamical state of the planetesimals does not seem to affect the outcome of accretion, so it is safe to assume that the resulting distribution of proto-**

planets would remain unchanged had we started with a colder disk. The viscous stirring timescale is given by Ida & Makino (1993) as

$$t_{vs} = \frac{\langle e^2 \rangle}{d \langle e^2 \rangle / dt} \approx \frac{1}{40} \left(\frac{\Omega^2 a^3}{2 G m_{pl}} \right)^2 \frac{4 m_{pl} \langle e^2 \rangle^2}{\Sigma a^2 \Omega}, \quad (12)$$

where Ω, a and e are the orbital frequencies, semi-major axes and eccentricities of the individual planetesimals, **respectively. In the Stokes regime, where the mean-free path of the gas is much smaller than the solid particles, the gas can be treated as a fluid and** the drag timescale is given by Adachi et al. (1976) as

$$t_s = \frac{2 m_{pl}}{C_D \pi r_{pl}^2 \rho_g v_g}, \quad (13)$$

where C_D is a drag coefficient of order unity, ρ_g is the local gas volume density and v_g is the headwind velocity of the gas experienced by the planetesimal. The local gas volume density is given by

$$\rho_g = \frac{\Sigma_g}{\sqrt{2\pi} h_g} \exp\left[-z^2 / \left(2 h_g^2 \right) \right], \quad (14)$$

where Σ_g is the gas surface density (taken to be 240 times the solid surface density (Hayashi 1981), $h_g = c_s/\Omega$ is the local gas scale height and z is the height above the disk midplane. The sound speed profile is given by $c_s = \sqrt{k_B T(r) / (\mu m_H)}$, where k_B is Boltzmann's constant, $T(r) = T_0 \left(r/1\mathrm{AU} \right)^{-q}$, $\mu = 2.34$ and m_h is the mass of a hydrogen atom. For a protoplanetary disk around a typical M star, $T_0 = 148$ K and $q = 0.58$ (Andrews & Williams 2005).

Finally, the headwind velocity of the gas, due to the fact that the gas disk is pressure supported, is given by

$$v_g = v_k \left[1 - \sqrt{q c_s^2 / v_k^2} \right], \quad (15)$$

where v_k is the local Keplerian velocity **(see eq. 4.30 of** Armitage (2020)**)**. As in section 4, the argument of perihelion ω, longitude of ascending node Ω, and mean anomaly M for the planetesimals are drawn from a uniform distribution $\in [0, 2\pi)$.

One should note that this choice for the gas disk profile almost certainly does not capture the wide range of possibilities in real planet-forming disks. On one hand, a larger initial gas surface density could act to completely remove solids via radial drift, rendering in-situ accretion of solids impossible. On the other hand, a more tenuous gas disk might render aerodynamic drag forces completely unimportant. In this case, the random velocity of the initial planetesimals should

be close to their mutual escape velocity. As we showed in section 4, the initial dynamical state of the solids seems to have a very minimal effect on the final outcome of planetesimal accretion. In a similar vein to Hansen & Murray (2012), we choose to use a MMSN-like profile for the gas disk and instead vary the solid surface density profile to capture the range of mechanisms that might have acted to facilitate planetesimal formation in the first place.

5.2. *Gas Drag Force*

In addition to the mutual gravitational forces, a Stokes drag force due to the the gas disk is applied to each particle, following the prescription described in section 2.2.1 of Morishima et al. (2010). For the initial mass planetesimals, the **Stokes number ($St = t_s\Omega$) at the inner and outer disk edge is roughly 2×10^5 and 10^7, respectively. For $\tau_s \gg 1$, bodies are decoupled from the gas and are only weakly affected by it. Because $\tau_s \sim m^{1/3}$, the Stokes number grows as planetesimal accretion proceeds, and the drag force plays an increasingly minor role.** Although the aerodynamic gas drag is not expected to significantly alter the final protoplanet distribution, we include its effects here to be self-consistent with the initial conditions, which were constructed by balancing the effects of viscous stirring with gas drag.

5.3. *Timestepping Criterion*

In the case of the fdHi simulation, there are nearly 1 million particles, whose orbital periods vary by two orders of magnitude. Because the interaction timescales near the inner edge of the disk are exceedingly short, a fixed timestep size would required a prohibitively large number of steps to follow planetesimal growth throughout the entire disk. For this reason, we use a multi-tiered timestepping scheme, in which particles are placed onto the nearest power of two timestep based on their most recently calculated gravitational acceleration. **This scheme is used on almost all works using ChaNGa, and is common among large-scale simulation codes.**

This more efficient scheme introduces two issues, however. Firstly, momentum is not completely conserved when bodies switch timestep tiers. The error introduced becomes particularly severe for a particle on an eccentric orbit, whose perihelion and aphelion distances straddle a timestep boundary. For a large collection of particles, this problem manifests itself as the development of a V-shaped gap in the a-e plane, centered on the boundary itself. To correct this problem, we introduce a slightly modified timestepping criterion, which is based on the expected gravitational acceleration of the particle at pericenter. Only in the case of a close encounter with another planetesimal (in which the acceleration is no longer dominated by the star) is the timestep allowed to reduce based on the original instantaneous criterion.

A second issue is introduced when two particles on different timesteps undergo a collision. As in the previous case, momentum is not completely conserved because the most recent 'kick' steps did not happen simultaneously for these bodies. Early in the simulation, we find that this problem tends to trigger runaway growth at the timestep boundaries first. This issue carries itself forward through the embryo formation phase, and protoplanets tend to form at the boundaries. To correct this issue, we ignore collisions between bodies on different timesteps early in the simulation. We find that preventing multi-timestep collisions until after the maximum mass grows by a factor of 10 prevents any artifacts from developing at the timestep boundaries, while also minimizing the number of 'skipped' collisions. **In the case of the fdHi simulation, only about 20 collisions out of an eventual 900,000 are ignored. To verify that this timestepping scheme does not affect protoplanet growth, we tested an annulus of growing planetesimals with both fixed steps and our two-phase variable timestepping scheme. The results of these tests are shown in appendix A.**

5.4. *Results*

The timescales for embryo formation depend on the chosen surface density profile, along with the local orbital timescale. Protoplanets form first at the inner edge of the disk, where the dynamical timescales are short. Growth proceeds in an inside-out fashion, with the outermost regions of the disk completing the protoplanet assembly phase last **(as an example, see figure 1 of Kokubo & Ida (2002)**. This radial timescale dependence is not typically accounted for in planet formation simulations **(a notable exception being Emsenhuber et al. (2021a,b))**, and appears to be an important component to forming realistic solar system analogs (Clement et al. 2020). As with the narrow annulus simulations, we stop the integration once the masses of protoplanets in the outermost region of the disk reach a steady value. In table 1, we summarize the outcomes of the four "full disk" cases.

We show the final state of the "fdHi" simulation in figure 5. In the top panel, the initial (contours) and final (points) state of the simulation is shown in the orbital period-eccentricity plane. The size of the points

Table 1. Summary of Full Disk Simulations

Simulation Name	$m_{pl}[M_\oplus]$	N_{pl}	A	δ	$M_{PP}[M_\oplus]$	$T_{int}[yr]$	$T_{int,1}[yr]$
fdHi	8.37×10^{-6}	903,687	100	1.5	1.00	456	16,377
fdHiSteep	8.37×10^{-6}	903,687	100	2.5	1.19	456	16,377
fdHiShallow	8.37×10^{-6}	903,687	100	0.5	1.08	456	16,377
fdLo	8.37×10^{-6}	45,185	1	1.5	1.77×10^{-3}	3,713	133,651

A summary of the four 'full disk' simulations presented in section 5. m_{pl} and N_{pl} are the initial masses and number of planetesimals. A and d is the initial power law normalization and slope of the solids in the disk. M_{PP} is the maximum protoplanet mass at the end of the simulation and T_{int} is the amount of time each simulation was integrated. $T_{int,1}$ is the integration time scaled by a factor of f^2, which accounts for the fact that the accretion timescale has been shortened by the inflated collision cross sections.

Text goes here
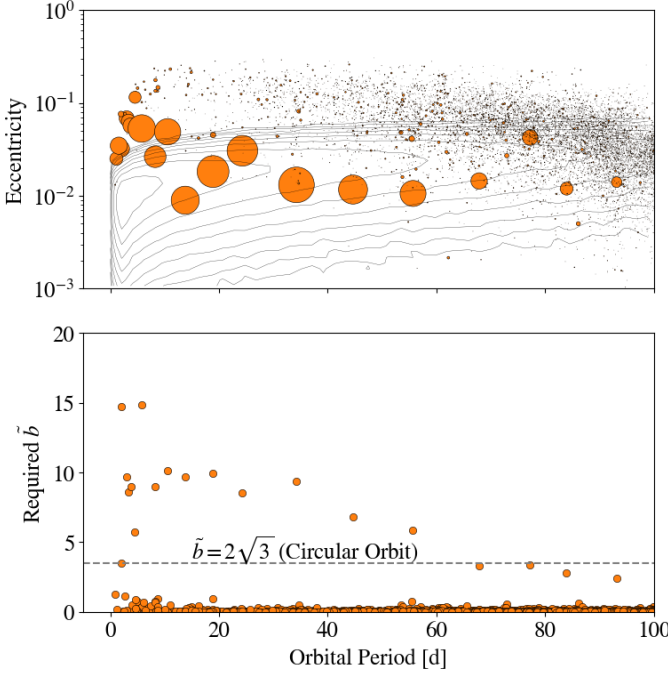
Figure 5. The final state of the fdHi simulation. In the top panel, the contours denote the initial period-eccentricity distribution of the planetesimals. Point sizes indicate the relative masses of bodies at the end of the simulation. In the bottom panel, we show the feeding zone width (see equation 8) required to produce the final masses of the bodies. The dashed line indicates the feeding zone size expected for bodies on circular orbits. **For the shorter period bodies, the feeding zone size exceeds this expected value, which indicates that oligarchic growth is not operating here. This boundary occurs near roughly 60 d in orbital period.**

790 indicates the relative mass of the bodies. In the bottom
791 panel, the final masses of the bodies (in units of feeding
792 zone size) are shown as a function of orbital period. **The**
793 **y-values in the bottom panel of figure 5 are cal-**
794 **culated by solving equation 8 for $\tilde{b}$, and inputting**
795 **the initial surface density and final particle mass**
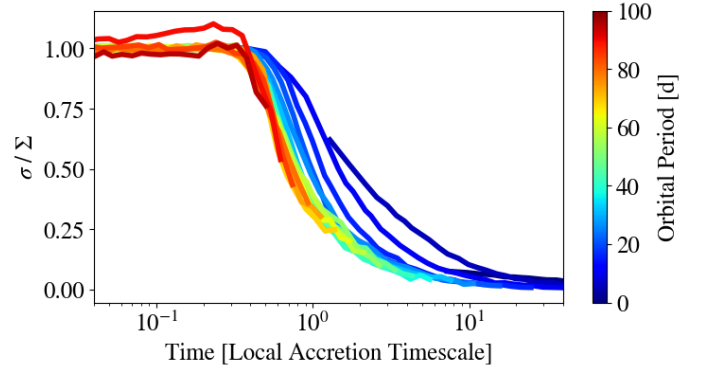
Figure 6. The time evolution of the planetesimal surface density (in units of the total solid surface density) in the fdHi simulation. Each curve represents a radial slice of the disk. **The time is measured in units of the local accretion timescale at the center of each radial zone. The colors represent the orbital period at the center of each zone.**

796 **into the expression.** Here, we assume that each em-
797 bryo has reached its isolation mass, and that differences
798 in mass are driven by differences in the initial surface
799 density at the embryo's current location, along with the
800 size of its feeding zone, which is set by the dynamics
801 relevant at that location in the disk. By plotting the
802 derived value of $\tilde{b}$ as a function of orbital period, differ-
803 ences in the dynamical interactions at different locations
804 of the disk are made more clearly visible. **The feeding**
805 **zone size $\tilde{b} = 2\sqrt{3}$ permitted by bodies on circu-**
806 **lar, non-inclined orbits (Nakazawa & Ida 1988)**
807 **is shown by the horizontal dashed line.** In typi-
808 cal oligarchic growth simulations (Kokubo & Ida 1998),
809 protoplanets tend to space themselves apart by $\tilde{b} = 10$,
810 although it should be noted that they do not consume
811 all of the planetesimals within this distance.
812   A qualitative shift in the protoplanet and planetesimal
813 distribution is visible **inside of** ~ 60 days. Interior to
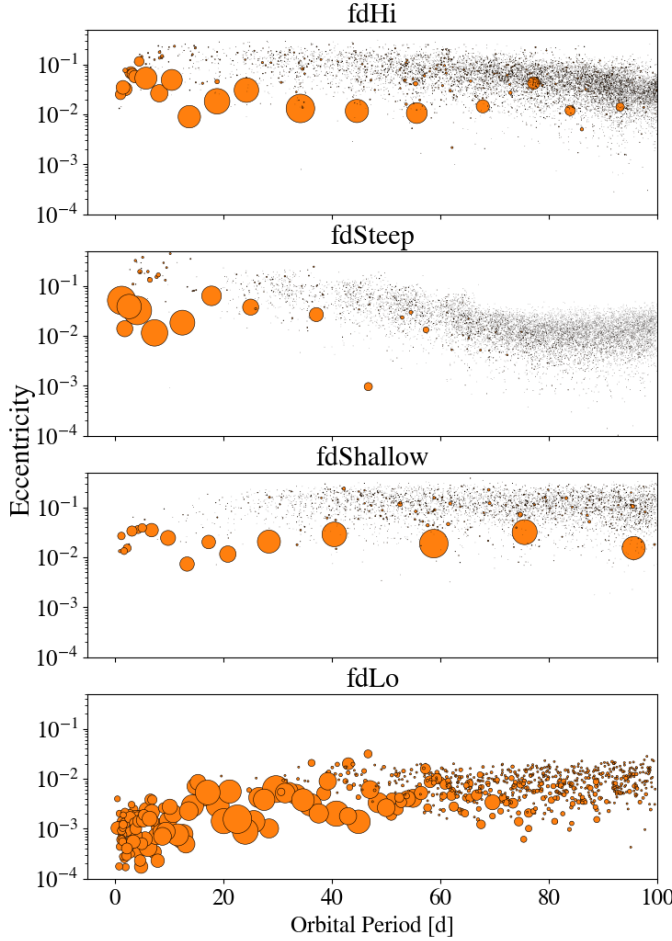814 this location, there are very few remaining planetesimals

Figure 7. The final state of the full disk simulations listed in table 1. Point sizes indicate mass relative to the largest body in each simulation.
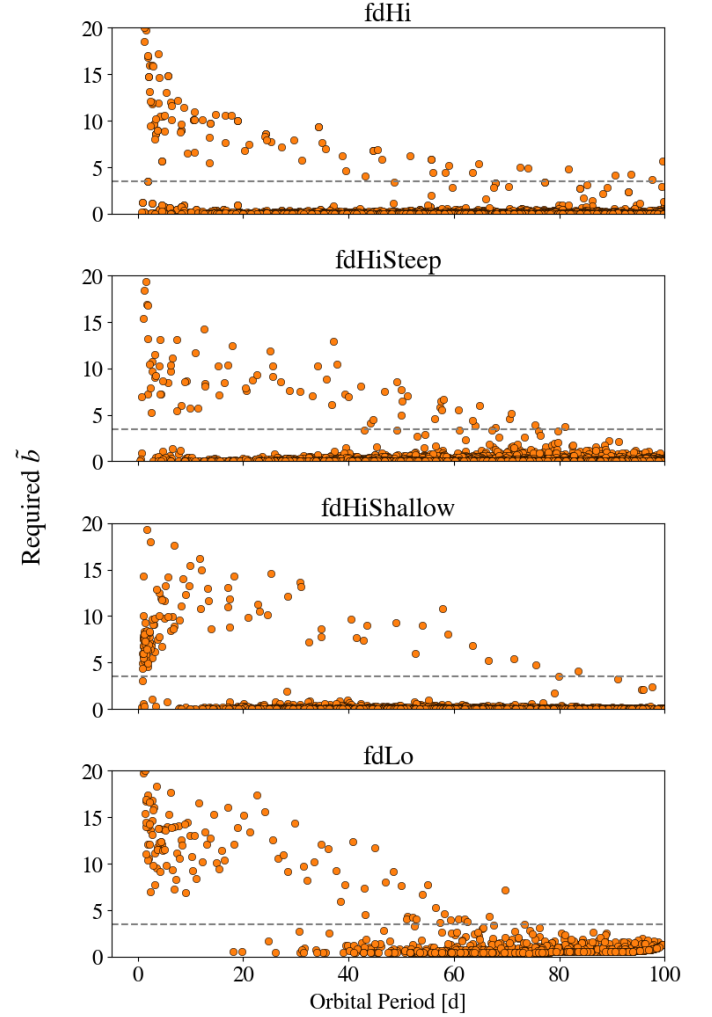
and the embryos formed have larger feeding zones. Exterior to the boundary, the residual planetesimal population is much more visible, and protoplanets more closely follow the $\tilde{b} = 2\sqrt{3}$ line. This suggests that the transition between the low α and high α accretion modes seen in section 4 is happening near this location.

In section 4, we postulated that the increased importance of inelastic damping in the inner, non-oligarchic growth region of the disk should lower the overall eccentricity of the protoplanets there. This behavior is not immediately apparent in the top panel of figure 5. There are, however, a couple of factors in the wide disk simulations that could make this extra dynamical cooling mechanism difficult to see. Firstly, the initial eccentricity distributions of the inner and outer disk are different because of the dependence of the viscous stirring and gas drag timescales on orbital period. **The mean eccentricity at the outer disk edge is 4x larger than at the inner disk edge.** Additionally, the protoplanet

Figure 8. Feeding zone width (see equation 8) required to produce the final masses for the protoplanets from the simulations listed in table 1. **For the fdHi, fdHiSteep and fdHiShallow simulations, we have included the results from five separate iterations of the simulations, each using a different random number seed.** The horizontal dashed line indicates $\tilde{b} = 2\sqrt{3}$. Despite the vastly different initial solid surface density profiles, the feeding zone width reaches the circular orbit value around ~ 60 days in all cases.

formation timescales for the inner and outer disk are vastly different, making a comparison between these regions at the same moment in time somewhat inappropriate.

To ensure that the boundary seen **around** 60 days in orbital period is not simply a transient product of the inside-out growth throughout the disk, we examine the time evolution of σ/Σ, which compares the planetesimal and total solid surface density at multiple orbital periods. In figure 6, the value of σ/Σ is plotted as a func-

tion of time in 10 orbital period bins, each with a width of 10 days. **To determine whether the evolution of the planetesimal surface density behaves self-similarly across the disk, we normalize the time values in each bin by the local accretion timescale at the beginning of the simulation, which is given by**

$$t_{acc} = (n\Gamma v)^{-1} = \left(\frac{\Sigma_0 \Omega}{2m_{pl}}\Gamma\right)^{-1}, \qquad (16)$$

where we have assumed the local number density of particles n is set by the surface density and the local scale height of the disk (see section 2). The effective collision cross section is set by gravitational focusing and is given by equation 5.

The color of the curves indicate the orbital period bin which is being measured. From about 40 to 100 days in orbital period, the planetesimal surface density follows a similar trajectory as accretion proceeds. Interior to about 40 days, σ actually decays more slowly. In other words, growth is actually fueled less vigorously by planetesimals in this region. This highlights the fact that accretion proceeds in a qualitatively different way in the inner disk. For the outer disk, gravitational focusing tends to facilitate collisions between protoplanets and preferentially smaller bodies. At short period, however, all close encounters result in a collision, regardless of mass. In a rather counterintuitive fashion, planetesimals in the inner disk actually persist for longer. In section 5.5, we examine the assembly history of the embryos and show that there is much less of a preference for planetesimal-embryo collisions at short period as well.

In the inner disk, this value asymptotes to zero as the planetesimal population entirely depletes. In the outer disk, dynamical friction between the embryos and planetesimals eventually throttles subsequent accretion and leaves ~ 10 percent or more of the mass surface density as planetesimals. **It should be noted that in a typical oligarchic growth scenario, where protoplanets space themselves apart by 10 r_h and settle onto circular orbits (giving $\tilde{b} = 2\sqrt{3}$), roughly 30 percent $(2\sqrt{3}/10 \simeq 0.3)$ of the planetesimals should remain out of reach of the protoplanets.**

Next, we investigate how the resulting planetesimal and protoplanet distribution changes as we vary the initial solid surface density profile. The final orbital period-eccentricity state of the particles in the fdHi, fdHiSteep, fdHiShallow and fdLo simulations are shown in figure 7, with point sizes indicating the relative masses of the bodies. In all cases, the inner disk is largely depleted of planetesimals, while the outer disk contains a bimodal population of planetesimals and embryos, with a clear separation in eccentricity between the two. Despite having significantly different masses, the **semi-major axis-eccentricity** distributions of the planetary embryos formed in all simulations **are** remarkably similar. This is likely due to the fact that inelastic collisions play a more significant role where the solid surface density is highest, which offsets the fact that the initial bodies started off in a dynamically hotter state (due to the increased effectiveness of viscous stirring). The only exception to this is the fdLo simulation, where the resulting eccentricities are a couple orders of magnitude smaller. Inelastic damping likely plays an even more significant role here, due to the much larger masses of the initial planetesimals.

In figure 8, we plot the masses of the resulting protoplanets and planetesimals in all four simulations in units of $\tilde{b}$ (see equation 8). **To make the trend between $\tilde{b}$ and orbital period more clear, we ran four more versions of the fdHi, fdHiSteep and fdHiShallow simulations using different random number seeds and included these in the figure as well.** As mentioned previously, $\tilde{b} = 2\sqrt{3}$ (indicated by the horizontal dashed line) is the feeding zone width that a body on a circular orbit will have. In all four simulations, the feeding zone width exceeds the minimum value in the inner disk and approaches $2\sqrt{3}$ **around $\sim$ 40 to 60 days**. The orbital periods at which this transition occurs are quite similar between simulations, despite the vastly different solid surface density profiles used. This indicates that the boundary between accretion modes is driven entirely by the local value of α, and also supports our conclusion that planetesimal accretion is largely complete everywhere in the disk.

5.5. *Assembly History of Embryos*

Further insight regarding the difference between the short vs long period accretion modes can be gained by looking at the growth history of the planetary embryos. Because all collisions are directly resolved by the N-body code, a lineage can be traced between each planetary embryo and the initial planetesimals.

We begin by investigating the "smoothness" of the accretion events that give rise to each embryo. Drawing from a common technique used for cosmological simulations of galaxy formation, we divide growth events for a given body into "major" and "minor" mergers (Kauffmann & White 1993; Murali et al. 2002; L'Huillier

et al. 2012). Here, we define minor events as any collision involving an initial mass planetesimal, while major events consist of a merger between any two larger bodies. **In figure 9, we retrieve the collision events for all bodies in all five iterations of the fdHi, fdHiSteep and fdHiShallow simulations and plot the total mass fraction attained through minor merger events as a function of the final mass of the body. Here, we define a minor merger to be any collision involving a planetesimal with** $m < 100m_0$. **The color of the points indicates the final orbital period of the body. Beyond** $\sim$ **20 to 30 days in orbital period, minor mergers make up a significant fraction of the final mass of a body. Interior to this, the smooth accretion fraction drops significantly and the mass contribution to minor mergers can vary by over an order of magnitude.**

The variation in smooth accretion fraction with mass for the short period bodies suggests that the planetesimal and embryo populations interact differently than those in the outer disk. Exterior to the accretion mode boundary, the growing embryos continue to accrete planetesimals **while avoiding each other** as they near their final mass. Inside the boundary, however, **any and all bodies collide with each other, and the occasional embryo-embryo collision tends to dominate growth and drive down the smooth accretion fraction.** Gravitational scattering between embryos and planetesimals is a key ingredient for orbital repulsion (Kokubo & Ida 1998), and so a lack of gravitational scattering in the inner disk should prevent the embryos from settling onto neatly-spaced, isolated orbits. As we showed in figure 8, the embryos in the inner disk appear to reach well beyond the typical feeding zone size predicted by an oligarchic growth model. Figure 9 suggests that the extra mass here obtain comes from mergers with the other nearby embryos.

Another line of evidence pointing to a lack of gravitational scattering and orbital repulsion in the inner disk can be seen in figure 10. **Here, we measure the initial orbital period distribution of bodies used to construct each embryo and calculate its mean** $\langle P_{acc} \rangle$. **Point sizes indicate the relative final masses of bodies. As in the previous figure, we have included data from all five versions of the fdHi, fdHiSteep and fdHiShallow simulations. For each body, this quantity is then compared with its final orbital period. In this figure, bodies that closely follow the gray dashed line still reside close to their initial feeding zones. On the other hand, bodies further from the dashed**
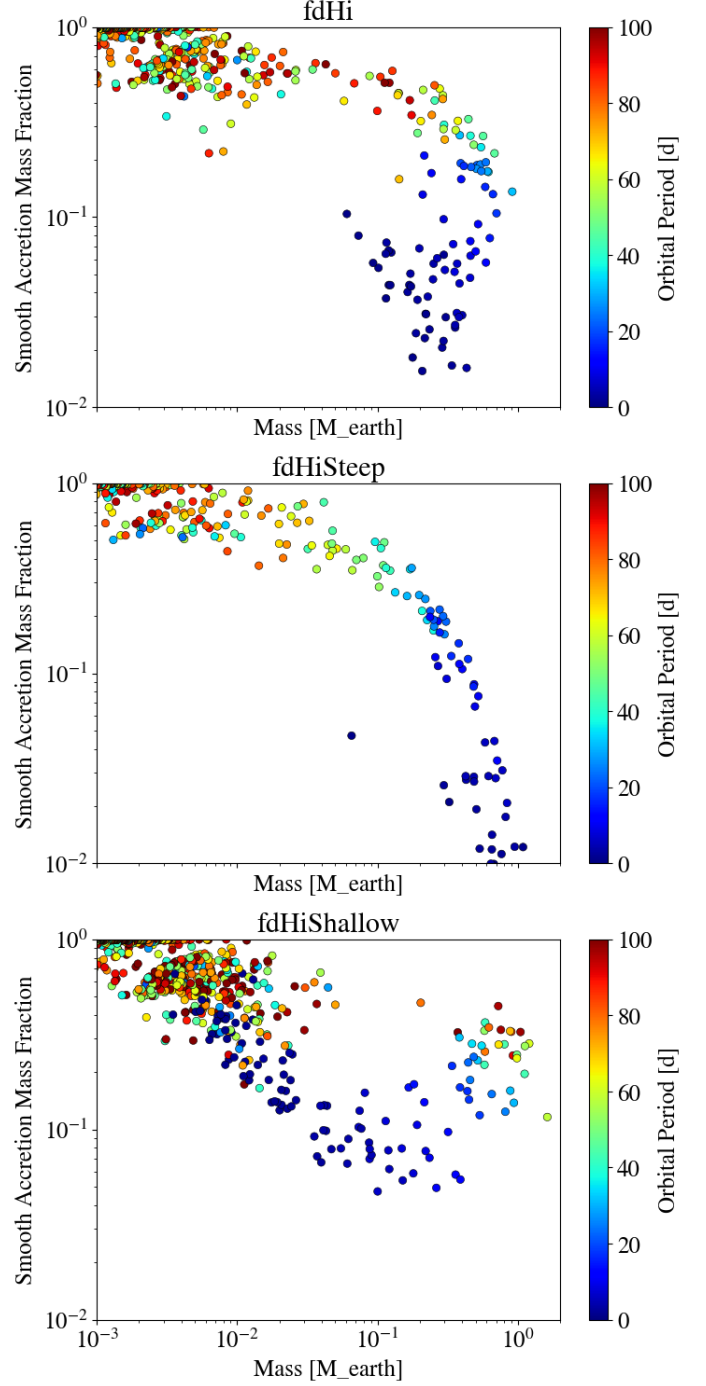
Figure 9. For all bodies with $m > 100m_0$ at the end of the high surface density simulations, the fraction of their total mass attained through mergers with initial mass planetesimals (smooth accretion) as a function of total mass. **Colors indicate the orbital periods of the bodies in the final simulation snapshot. Bodies interior to $\sim$ 20 to 30 days attain up to an order of magnitude less of their mass through minor merger events, while accretion of planetesimals plays a much more significant role at longer orbital periods.**
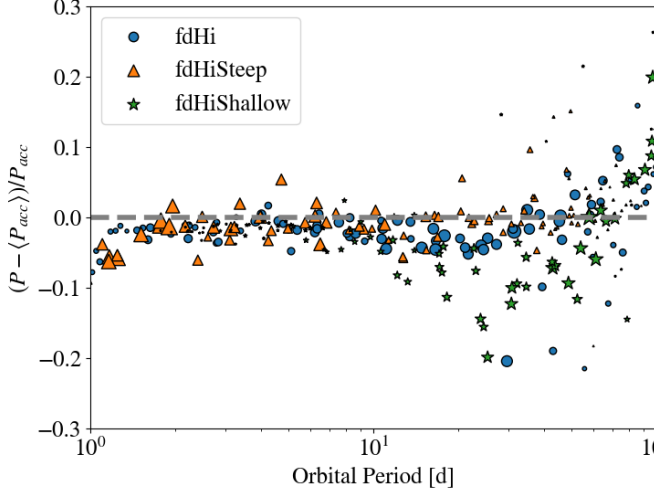
Figure 10. The relative separation between a body the mean orbital periods of its accretion zone at the end of the fdHi, fdHiSteep and fdHiShallow simulations. The marker type and color denotes the simulation used, while the marker sizes indicate the relative masses of bodies. In each case, all five iterations of the simulations are plotted simultaneously.

line must have experienced a strong gravitational scattering event during or after their accretion has completed. For all of the high surface density simulations, the accretion zones and present positions of the embryos appear to diverge beyond ∼ 20 days in orbital period.

Coupled with the strong decrease in smooth accretion fraction for bodies in this region (seen in figure 9), it appears as if the relative importance of collisions and gravitational scattering seems to shift around ∼ 20 days. For the shortest period bodies, growth events are sudden and stochastic, often involving collisions between bodies of comparable mass. For longer period bodies, a significant amount of growth is driven by accretion of smaller planetesimals. We postulate that this qualitative difference is driven by the role that embryo-embryo close encounters play in the inner and outer disk. In the inner disk, these encounters tend to result in a merger, which drives down the smooth accretion fraction. In the outer disk, these encounters tend to result in a scattering event which moves bodies away from their initial feeding zones. We find that the accretion zone shapes for the longer period bodies are also much more smooth and unimodal, which suggests that scattering tends to occur after accretion has largely completed.

6. SIMPLIFYING ASSUMPTIONS

6.1. *Collision Cross Section*

In all cases shown so far, the boundary between the oligarchic growth and the highly-efficient short period accretion region lies **between 40 and 70** days in orbital period. As discussed in section 2.2, the mode of accretion is set entirely by the local value of α, which scales with both distance from the star and the bulk density of the planetesimals (see equation 9). Because we chose to artificially inflate the collision cross section of the particles in our simulations **by a factor of** f, the bulk densities of the particles are reduced, and the accretion boundary is shifted outward. However, the scaling relation between α and ρ ($\alpha \sim \rho_{pl}^{-1/3}$) can be used to predict where this accretion boundary should lie in a disk with realistic-sized planetesimals. The simulations presented in this paper use a collision cross section enhancement factor of 6, which moves the boundary outward in orbital period by a factor of approximately 15 (**For a fixed value of** α, **equation 9 gives** $a \sim r_{pl} \sim f$ **and therefore** $P_{orbit} \sim f^{-3/2}$). One would therefore expect the accretion boundary to lie **between 3 and 5 days** in orbital period for 3 g cm^{-3} bodies.

Although a simulation with $f = 1$ is not computationally tractable, we can test whether the accretion boundary moves in the way we expect by modestly changing the value of f. In figure 11, we compare the fdHi simulation to a nearly identical run using $f = 4$. In the top panel, we show the feeding zone width required for each particle to attain its present mass. As in figure 8, we indicate the feeding zone size expected for oligarchic growth with a horizontal dashed line. In the bottom panel, the value of α as a function of orbital period is shown for 3 g cm^{-3} bodies with an artificial radius enhancement of $f = 1, 4$ and 6. The horizontal dashed line indicates the empirical value of alpha below which the accretion mode switches to oligarchic. Comparing the top and bottom panels, the intersection of the feeding zone width seen in our simulations and the feeding zone width predicted by oligarchic growth matches well with the orbital period at which $\alpha \sim 0.1$ for both values of f. Also shown by the shaded region are the expected α values for realistic-sized bodies with ρ_{pl} between 1 and 10 g cm^{-3}. Although the removal of the cross section enhancement greatly reduces the size of the non-oligarchic region, it still should be expected to cover a portion of the disk where planetesimals might be expected to form (Mulders et al. 2018) for a wide range of ρ_{pl}.

6.2. *Collision Model*

For the simulations presented in this work, every collision results in a perfect merger between pairs of bod-
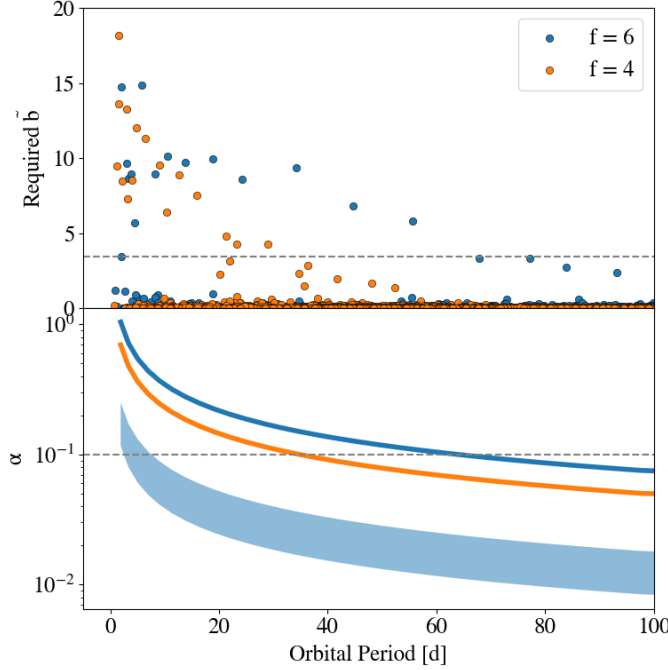
Figure 11. In the top panel, we show the required feeding zone sizes to produce the masses of the bodies seen at the end of the fdHi and fdHif4 simulations. The bottom panel shows the variation of α with orbital period for the bodies used in each case (solid curves). The orbital period at which $\alpha \simeq 0.1$ matches well with the location at which $\tilde{b}$ exceeds $2\sqrt{3}$. The shaded region in the bottom panel show the values of alpha for realistic-sized ($f = 1$) planetesimals with bulk densities between 10 and 1 g cm^{-3}.
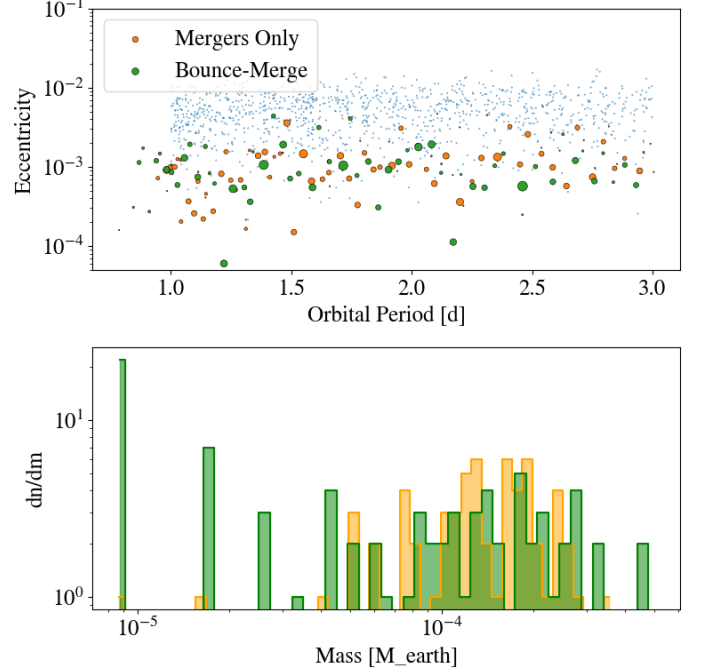
Figure 12. A comparison between the innermost region of the fdLo (orange) simulation, and a second version using a bounce- merge collision model (green). In the top panel, the period-eccentricity state of the particles is shown, with marker sizes indicating relative mass. The blue points represent the initial state of the simulations. The bottom panel compares the final **differential** mass distributions of the bodies.

ies, with no loss of mass or energy. Although simpler and less computationally expensive to model, allowing every collision to produce a perfect merger might result in overly efficient growth, particularly in the innermost region of the disk where the encounter velocities are largest. **Given that we have just shown that a distinctly non-oligarchic growth mode emerges in the inner disk when the collision timescale is short relative to the gravitational scattering timescale, one might be concerned that a more realistic collision model would act to lengthen the growth timescale enough for this condition to no longer be true. In the outer regions of the disk where oligarchic growth still operates, more realistic collision models have been shown to simply lengthen the timescale for planetary embryos to form (**Wetherill & Stewart 1993; Leinhardt & Richardson 2005**).** A proper way to handle this would be to allow for a range of collision outcomes, based on a semianalytic model (see Leinhardt & Stewart (2012)). However, resolving collisional debris, or even prolonging

Figure 13. The evolution of the ratio between the maximum and mean mass of the simulations shown in figure 12. In both cases, the system first evolves through a phase of runaway growth, before the massive bodies consume the smaller bodies, driving down the mean mass. With the bounce-merge model, the mass ratio takes much longer to begin decreasing.

growth by forcing high-velocity pairs of bodies to bounce is too expensive to model, even with CʜᴀNGᴀ.

To test whether a more restrictive collision model should alter the growth mode of the inner disk, we ran a smaller scale test using a more restrictive collision model. In this case, a collision can result in one of two outcomes: if the impact velocity is smaller than the mutual escape velocity of the colliding particles, defined as

$$v_{mut,esc} = \sqrt{\frac{2G(m_1 + m_2)}{r_1 + r_2}}, \tag{17}$$

where m_1, m_2 and r_1, r_2 are the masses and radii of colliding particles 1 and 2, then the bodies merge. For impact velocities larger than $v_{mut,esc}$, no mass is transferred, and the bodies undergo a completely elastic bounce. Because the accretion outcome is all or nothing, this model should restrict growth more than a partial accretion model (Leinhardt & Stewart 2012). Below, we will show that the bounce-merge model does not meaningfully affect the outcome of the inner disk's planetesimal accretion phase, and so a more realistic partial accretion model should do the same.

To compare the outcome of the two collision models, we have chosen to use the initial conditions from the fdLo simulation, but have truncated the disk beyond 3 days in orbital period. This offsets the increased computational cost of the more restrictive collision model, while still allowing the disk to evolve in the region where mergers would be most difficult to achieve. For the initial conditions we have chosen, the typical encounter velocity (defined by $v_{enc} = \langle e^2 \rangle^{1/2} v_k$, where v_k is the local Keplerian velocity) is about 25 percent larger than $v_{mut,esc}$. Because the encounter velocities follow a Gaussian distribution, there should still be a small subset of collisions that still meet the merger criteria to occur early on. In addition, $v_{mut,esc}$ becomes larger as the bodies grow and the merger criteria should become easier to meet as the system evolves. For these reasons, one would expect the inhibition of growth due to the more restrictive collision model to be temporary.

In figure 12, we compare the outcomes of the simulations, one with mergers only (shown in orange) and one with the bounce-merge model (shown in green). The blue points in the top panel show the initial conditions used for both cases. Although the bounce-merge simulation takes much longer to reach the same phase of evolution, the resulting orbital properties are indistinguishable from the merger-only case. **Performing a Kolmogrov-Smirnov test on the two mass distributions yields a p-value of 2×10^{-5}, which tells us that the two mass distributions are quite firmly statistically different. If we remove the initial mass planetesimals, a KS test yields a p-value of 0.1. We conclude that the embryo populations are nearly indistinguishable, but the bounce-merge model produces a small amount of residual planetesimals.**

To investigate the differences in growth between the two collision models early on, we show the time evolution of the ratio between the maximum and mean mass in figure 13. In both cases, this ratio first increases, which indicates that runaway growth still operates, regardless of the collision model used. In the bounce-merge case, the mass ratio peaks at a higher value, while also undergoing a longer runaway growth phase. This suggests that the mass distribution becomes much less unimodal during this growth process, but as figure 12 shows, this does not affect the resulting embryos or allow for a residual planetesimal population.

As a final note, Childs & Steffen (2022) found that a more realistic collision model also enhanced radial mixing in their simulations. Upon calculating the planetesimal accretion zones using the same method as was done to produce figure 10, we find that the embryos in the bounce-merge simulation annulus do have modestly wider accretion zones than those produced in the merger-only simulation.

7. SUMMARY AND DISCUSSION

In this work, we have demonstrated that planetary embryo growth can simultaneously operate in two distinct modes in a planet-forming disk. In the first mode, gravitational feedback from the growing embryos heats the remaining planetesimals and results in a dynamically cold population of embryos with a modest amount of residual planetesimals. This corresponds to the "oligarchic growth" case revealed by (Kokubo & Ida 1998), which is often used as a starting point for late-stage accretion models (e.g. Kokubo & Ida (2002); Raymond et al. (2005, 2006)). In the second mode, the gravitational feedback does not **play a significant role**, embryos quickly sweep up all planetesimals, and grow larger and less uniformly spaced than those produced by oligarchic growth.

We have demonstrated the outcome of both accretion modes through a simple parameter study using a narrow annulus of planetesimals **(section 4)**. The initial planetesimal distribution can be described in terms of two dimensionless constants, α and β, which describe the ratio between the physical radius of the planetesimals and the Hill (r_h) and gravitational (r_g) radius, respectively. For a fixed planetesimal composition, α scales with the orbital period and β scales with the level of dynamical excitation of the disk. We showed that $\alpha \ll 1$ leads

to oligarchic growth, while **an α close to unity** produces this newly revealed non-oligarchic growth mode **(see figure 2)**. Within this non-oligarchic mode, we find that the resulting masses and eccentricities of the embryos come out **very similar**, regardless of the initial value of β.

So long as the density of the bodies do not significantly change as their mass distribution evolves, this ratio is set entirely by the distance from the star. Because both the physical and Hill radii of the bodies grows as $M^{1/3}$, the growth mode boundary remains stationary in the disk during the planetesimal accretion process.

We have verified that the growth boundary location **does not strongly depend** of the solid surface density distribution by testing the outcome of the planetesimal accretion process for a variety of solid profiles. Although altering the surface density does affect the resulting masses of the embryos, the location of the boundary separating the growth modes is remarkably similar among all of our simulations. In addition, the sizes of the feeding zones, along with qualitative differences in the accretion history of embryos on both sides of the boundary **(see figures 9 and 10)** provide further evidence to suggest that oligarchic growth is not operating in the inner disk.

Finally, we have examined how our assumption of perfect accretion, along with the collision cross section enhancement used, might alter our results. We verified that these modifications, meant to make the simulations less computationally expensive, would still allow for the emergence of this non-oligarchic growth mode. We showed that a much more restrictive collision model, in which only low-velocity collisions produce a merger, still allows for this growth mode to occur at the innermost part of the disk, where encounter speeds are most vigorous. In a real planet-forming disk, partial accretion events should allow growth to happen more quickly than what was seen in this test case **(see figure 8 of Leinhardt et al. (2015))**, so this growth mode should certainly still occur. We also showed that the collision cross section enhancement moves the accretion boundary outward. We verified this by deriving a scaling relation between the boundary location and the bulk density of the planetesimals, and showing that the boundary moves to the predicted location when running a simulation with a slightly smaller inflation factor. For rocky planetesimals with a realistic bulk density **3 g cm^{-3}**, **our results suggest that** this boundary should lie around 5 days in orbital period.

7.1. *Connections to Satellitesimal Accretion*

To date, there have been no other studies of planetesimal accretion with such a large value of α. **Typically, it is assumed that $\alpha \ll 1$ (e.g. Lithwick (2014)), which is certainly true for material at and beyond the Earth's orbit.** However, a value of $\alpha = 1$ corresponds to the Roche limit of a three-body system, and so one might wonder this high-α accretion mode might be relevant for a circumplanetary accretion. There is a collection of previous works which use N-body methods to examine in-situ satellitesimal accretion (Ida et al. 1997; Richardson et al. 2000; Kokubo et al. 2000; Ida et al. 2020), although some of these simulations involve a complex interaction between spiral density waves formed inside of the Roche limit and the material exterior to it**, making the dynamics driving accretion distinctly non-local, in contrast to what we have presented in this work**. Ida et al. (1997) was able to form 1-2 large moons just exterior to the Roche limit, depending on the extent of the disk with very little satellitesimal material left over. The widest disk they modeled extended out to $\alpha = 0.5$. Qualitatively, this result is very similar to the short period planetesimal accretion mode observed in our simulations. Ida et al. (2020) modeled a much wider satellitesimal disk, which extends out to about $\alpha \approx 0.05$. Inside to the $\alpha = 0.1$ accretion boundary (which lies near 15 **planetary radii** in figure 1 of Ida et al. (2020)), bodies grow beyond the isolation mass, while the opposite is true on the other side of the boundary. In addition, a residual population of satellitesimals is still present beyond the boundary, which suggests that oligarchic growth is indeed operating only on the far side.

Presently, the implications that this non-oligarchic accretion mode has for the formation of short-period terrestrial planets, and whether the accretion boundary would leave any lasting imprint on the final orbital architecture, is unclear. The extreme efficiency of planetesimal accretion at the inner edge of the disk suggests that no residual populations of small bodies should be expected to exist here. A crucial point that our results do highlight is that the initial conditions used for most late-stage planet formation simulations are overly simplistic. Clement et al. (2020) recently simulated planetesimal accretion in a disk extending from the orbit of Mercury to the asteroid belt and found that the disk never reaches a state in which equally-spaced, isolation mass embryos are present everywhere simultaneously. Instead, different annuli reach a 'giant impact' phase at different times, preventing the onset of a global instability throughout the entire disk, as is common in classic terrestrial planet formation models (Chambers & Wetherill 2001; Raymond et al. 2009).

To connect these accretion modes to the final orbital architecture, and to ultimately determine what implications an in-situ formation model has for the growth of STIPs, we will evolve the final simulation snapshots presented here with a hybrid-symplectic integrator for Myr timescales. The final distribution of planets formed, along with composition predictions generated by applying cosmochemical models to our initial planetesimal distributions and propagating compositions through the collision trees, will be examined in a follow-up paper.

ACKNOWLEDGEMENTS

Software: Astropy (Astropy Collaboration et al. 2013), CHANGA (Jetley et al. 2008; Menon et al. 2015), Matplotlib (Hunter 2007), NumPy (van der Walt et al. 2011), Pandas (Wes McKinney 2010), PYNBODY (Pontzen et al. 2013)

DATA AVAILABILITY

The data presented in this article are available on our GitHub repository, at https://github.com/spencerw/stip_planetesimal_paper.

APPENDIX

A. ROBUSTNESS OF TIMESTEPPING SCHEME

As described in section 3, CHANGA evolves the motions of the particles in the planetesimal disk using a multi-tiered timestepping scheme. Due to the extremely short dynamical timescale at the inner edge of the disk, the outer disk would require a prohibitive number of timesteps to reach the protoplanet phase using a fixed timestep scheme.To circumvent this, particles are evolved in discrete power-of-two timestep groups. In the event that a collision occurs between two particles on different timesteps, a slight error is introduced to the energy and angular momentum of the merged particle. Due to the nonlinear nature of the runaway growth phase, this slight error tends to trigger more subsequent collisions at the timestep boundary in the disk, and causes protoplanets to preferentially form at the boundaries.

To circumvent this issue, we prohibit particles on different timesteps from merging until the runaway growth phase is well underway. For the fdHi simulation, multi-tiered mergers are not allowed during the first thousand steps. To verify that this technique does not alter the resulting protoplanet distribution in any meaningful way, we ran two test simulations of the inner part (1 to 4 days in orbital period) of the disk from the fdHi simulation. In the first case, the aforementioned timestepping scheme is used. In the second case, all particles are evolved on the timestep appropriate for the inner edge of the disk.

In figure 14, we compare the final period-eccentricity state and final mass distributions to each other. There do not appear to be any differences between the two protoplanet distributions, particularly near the timestep boundary at 2 days. In addition, the masses of both the protoplanets and the remaining growing planetesimals are indistinguishable. In this case, a KS test of the two mass distributions yields a p-value of ~ 0.34. We therefore safely conclude that the timestepping scheme used in this work does not alter the growth of the protoplanets in any meaningful way.

REFERENCES

Adachi, I., Hayashi, C., & Nakazawa, K. 1976, Progress of Theoretical Physics, 56, 1756, doi: 10.1143/PTP.56.1756

Agol, E., Dorn, C., Grimm, S. L., et al. 2021, PSJ, 2, 1, doi: 10.3847/PSJ/abd022

Andrews, S. M., & Williams, J. P. 2005, ApJ, 631, 1134, doi: 10.1086/432712

Andrews, S. M., Wilner, D. J., Hughes, A. M., Qi, C., & Dullemond, C. P. 2009, ApJ, 700, 1502, doi: 10.1088/0004-637X/700/2/1502

—. 2010, ApJ, 723, 1241, doi: 10.1088/0004-637X/723/2/1241

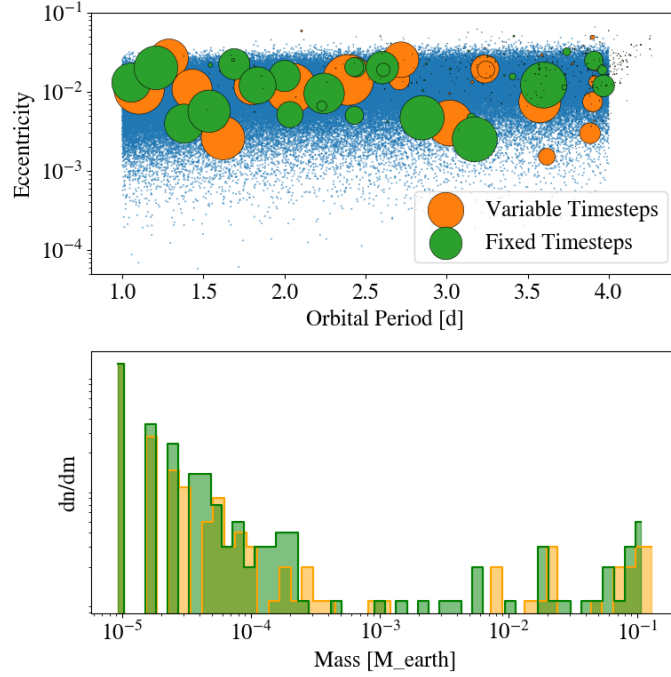Armitage, P. J. 2020, Astrophysics of planet formation, Second Edition

Figure 14. A comparison between the innermost region of the fdHi (orange) simulation, and a second version using a fixed timestep appropriate for the inner edge of the disk (green). In the top panel, the period-eccentricity state of the particles is shown, with marker sizes indicating relative mass. The blue points represent the initial state of the simulations. The bottom panel compares the final mass distributions of the bodies.

Astropy Collaboration, Robitaille, T. P., Tollerud, E. J., et al. 2013, A&A, 558, A33, doi: 10.1051/0004-6361/201322068

Bai, X.-N., & Stone, J. M. 2010, ApJ, 722, 1437, doi: 10.1088/0004-637X/722/2/1437

Baraffe, I., Homeier, D., Allard, F., & Chabrier, G. 2015, A&A, 577, A42, doi: 10.1051/0004-6361/201425481

Barnes, R., Quinn, T. R., Lissauer, J. J., & Richardson, D. C. 2009, Icarus, 203, 626, doi: 10.1016/j.icarus.2009.03.042

Beitz, E., Güttler, C., Blum, J., et al. 2011, ApJ, 736, 34, doi: 10.1088/0004-637X/736/1/34

Birnstiel, T., Fang, M., & Johansen, A. 2016, SSRv, 205, 41, doi: 10.1007/s11214-016-0256-1

Bitsch, B., Lambrechts, M., & Johansen, A. 2015, A&A, 582, A112, doi: 10.1051/0004-6361/201526463

Blum, J., & Münch, M. 1993, Icarus, 106, 151, doi: 10.1006/icar.1993.1163

Bottke, W. F., Durda, D. D., Nesvorný, D., et al. 2005, Icarus, 179, 63, doi: 10.1016/j.icarus.2005.05.017

Brauer, F., Henning, T., & Dullemond, C. P. 2008, A&A, 487, L1, doi: 10.1051/0004-6361:200809780

Chambers, J. E., & Wetherill, G. W. 1998, Icarus, 136, 304, doi: 10.1006/icar.1998.6007

—. 2001, M&PS, 36, 381, doi: 10.1111/j.1945-5100.2001.tb01881.x

Chiang, E., & Laughlin, G. 2013, MNRAS, 431, 3444, doi: 10.1093/mnras/stt424

Childs, A. C., & Steffen, J. H. 2022, MNRAS, 511, 1848, doi: 10.1093/mnras/stac158

Clement, M. S., Kaib, N. A., & Chambers, J. E. 2020, PSJ, 1, 18, doi: 10.3847/PSJ/ab91aa

Colwell, J. E. 2003, Icarus, 164, 188, doi: 10.1016/S0019-1035(03)00083-6

Drkażkowska, J., & Dullemond, C. P. 2018, A&A, 614, A62, doi: 10.1051/0004-6361/201732221

Drkażkowska, J., Windmark, F., & Dullemond, C. P. 2013, A&A, 556, A37, doi: 10.1051/0004-6361/201321566

Duncan, M., Quinn, T., & Tremaine, S. 1989, Icarus, 82, 402, doi: 10.1016/0019-1035(89)90047-X

Emsenhuber, A., Mordasini, C., Burn, R., et al. 2021a, A&A, 656, A69, doi: 10.1051/0004-6361/202038553

—. 2021b, A&A, 656, A70, doi: 10.1051/0004-6361/202038863

Fabrycky, D. C., Lissauer, J. J., Ragozzine, D., et al. 2014, ApJ, 790, 146, doi: 10.1088/0004-637X/790/2/146

Gillon, M., Jehin, E., Lederer, S. M., et al. 2016, Nature, 533, 221, doi: 10.1038/nature17448

Gillon, M., Triaud, A. H. M. J., Demory, B.-O., et al. 2017, Nature, 542, 456, doi: 10.1038/nature21360

Hansen, B. M. S., & Murray, N. 2012, ApJ, 751, 158, doi: 10.1088/0004-637X/751/2/158

Hayashi, C. 1981, Progress of Theoretical Physics Supplement, 70, 35, doi: 10.1143/PTPS.70.35

Hunter, J. D. 2007, Computing in Science and Engineering, 9, 90, doi: 10.1109/MCSE.2007.55

Ida, S. 1990, Icarus, 88, 129, doi: 10.1016/0019-1035(90)90182-9

Ida, S., Canup, R. M., & Stewart, G. R. 1997, Nature, 389, 353, doi: 10.1038/38669

Ida, S., Kokubo, E., & Makino, J. 1993, MNRAS, 263, 875, doi: 10.1093/mnras/263.4.875

Ida, S., & Makino, J. 1993, Icarus, 106, 210, doi: 10.1006/icar.1993.1167

Ida, S., Ueta, S., Sasaki, T., & Ishizawa, Y. 2020, Nature Astronomy, 4, 880, doi: 10.1038/s41550-020-1049-8

Izidoro, A., Bitsch, B., Raymond, S. N., et al. 2021, A&A, 650, A152, doi: 10.1051/0004-6361/201935336

Izidoro, A., Ogihara, M., Raymond, S. N., et al. 2017, MNRAS, 470, 1750, doi: 10.1093/mnras/stx1232

Jetley, P., Gioachin, F., Mendes, C. Kale, L., & Quinn, T. 2008, Proceedings of IEEE International Parallel and Distributed Processing Symposium

Johansen, A., Blum, J., Tanaka, H., et al. 2014, in Protostars and Planets VI, ed. H. Beuther, R. S. Klessen, C. P. Dullemond, & T. Henning, 547

Johansen, A., Oishi, J. S., Mac Low, M.-M., et al. 2007, Nature, 448, 1022, doi: 10.1038/nature06086

Johansen, A., Youdin, A., & Klahr, H. 2009, ApJ, 697, 1269, doi: 10.1088/0004-637X/697/2/1269

Kauffmann, G., & White, S. D. M. 1993, MNRAS, 261, 921, doi: 10.1093/mnras/261.4.921

Klahr, H. H., & Bodenheimer, P. 2003, ApJ, 582, 869, doi: 10.1086/344743

Kokubo, E., & Ida, S. 1995, Icarus, 114, 247, doi: 10.1006/icar.1995.1059

—. 1996, Icarus, 123, 180, doi: 10.1006/icar.1996.0148

—. 1998, Icarus, 131, 171, doi: 10.1006/icar.1997.5840

—. 2000, Icarus, 143, 15, doi: 10.1006/icar.1999.6237

—. 2002, ApJ, 581, 666, doi: 10.1086/344105

Kokubo, E., Ida, S., & Makino, J. 2000, Icarus, 148, 419, doi: 10.1006/icar.2000.6496

Lambrechts, M., & Johansen, A. 2012, A&A, 544, A32, doi: 10.1051/0004-6361/201219127

—. 2014, A&A, 572, A107, doi: 10.1051/0004-6361/201424343

Latham, D. W., Rowe, J. F., Quinn, S. N., et al. 2011, ApJL, 732, L24, doi: 10.1088/2041-8205/732/2/L24

Leinhardt, Z. M., Dobinson, J., Carter, P. J., & Lines, S. 2015, ApJ, 806, 23, doi: 10.1088/0004-637X/806/1/23

Leinhardt, Z. M., & Richardson, D. C. 2005, ApJ, 625, 427, doi: 10.1086/429402

Leinhardt, Z. M., & Stewart, S. T. 2012, ApJ, 745, 79, doi: 10.1088/0004-637X/745/1/79

Levison, H. F., Morbidelli, A., Tsiganis, K., Nesvorný, D., & Gomes, R. 2011, AJ, 142, 152, doi: 10.1088/0004-6256/142/5/152

Levison, H. F., Morbidelli, A., Van Laerhoven, C., Gomes, R., & Tsiganis, K. 2008, Icarus, 196, 258, doi: 10.1016/j.icarus.2007.11.035

L'Huillier, B., Combes, F., & Semelin, B. 2012, A&A, 544, A68, doi: 10.1051/0004-6361/201117924

Lissauer, J. J. 1987, Icarus, 69, 249, doi: 10.1016/0019-1035(87)90104-7

Lissauer, J. J., & Stewart, G. R. 1993, in Protostars and Planets III, ed. E. H. Levy & J. I. Lunine, 1061

Lissauer, J. J., Ragozzine, D., Fabrycky, D. C., et al. 2011, ApJS, 197, 8, doi: 10.1088/0067-0049/197/1/8

Lithwick, Y. 2014, ApJ, 780, 22, doi: 10.1088/0004-637X/780/1/22

Lyra, W., Johansen, A., Klahr, H., & Piskunov, N. 2008, A&A, 491, L41, doi: 10.1051/0004-6361:200810626

Mamajek, E. E. 2009, in American Institute of Physics Conference Series, Vol. 1158, Exoplanets and Disks: Their Formation and Diversity, ed. T. Usuda, M. Tamura, & M. Ishii, 3–10

Menon, H., Wesolowski, L., & Zheng, G. e. a. 2015, Computational Astrophysics and Cosmology, 2, 1

Morbidelli, A., Bottke, W. F., Nesvorný, D., & Levison, H. F. 2009, Icarus, 204, 558, doi: 10.1016/j.icarus.2009.07.011

Morishima, R., Stadel, J., & Moore, B. 2010, Icarus, 207, 517, doi: 10.1016/j.icarus.2009.11.038

Mulders, G. D., Pascucci, I., Apai, D., & Ciesla, F. J. 2018, AJ, 156, 24, doi: 10.3847/1538-3881/aac5ea

Mundy, L. G., Looney, L. W., & Welch, W. J. 2000, in Protostars and Planets IV, ed. V. Mannings, A. P. Boss, & S. S. Russell, 355

Murali, C., Katz, N., Hernquist, L., Weinberg, D. H., & Davé, R. 2002, ApJ, 571, 1, doi: 10.1086/339876

Nakagawa, Y., Sekiya, M., & Hayashi, C. 1986, Icarus, 67, 375, doi: 10.1016/0019-1035(86)90121-1

Nakazawa, K., & Ida, S. 1988, Progress of Theoretical Physics Supplement, 96, 167, doi: 10.1143/PTPS.96.167

Pontzen, A., Roškar, R., Stinson, G., & Woods, R. 2013, pynbody: N-Body/SPH analysis for python. http://ascl.net/1305.002

Raymond, S. N., O'Brien, D. P., Morbidelli, A., & Kaib, N. A. 2009, Icarus, 203, 644, doi: 10.1016/j.icarus.2009.05.016

Raymond, S. N., Quinn, T., & Lunine, J. I. 2005, ApJ, 632, 670, doi: 10.1086/433179

—. 2006, Icarus, 183, 265, doi: 10.1016/j.icarus.2006.03.011

Raymond, S. N., Scalo, J., & Meadows, V. S. 2007, ApJ, 669, 606, doi: 10.1086/521587

Richardson, D. C. 1994, MNRAS, 269, 493, doi: 10.1093/mnras/269.2.493

Richardson, D. C., Quinn, T., Stadel, J., & Lake, G. 2000, Icarus, 143, 45, doi: 10.1006/icar.1999.6243

Rowe, J. F., Bryson, S. T., Marcy, G. W., et al. 2014, ApJ, 784, 45, doi: 10.1088/0004-637X/784/1/45

Safronov, V. S. 1969, Evoliutsiia doplanetnogo oblaka.

Sheppard, S. S., & Trujillo, C. A. 2010, ApJL, 723, L233, doi: 10.1088/2041-8205/723/2/L233

Shibaike, Y., & Alibert, Y. 2020, A&A, 644, A81, doi: 10.1051/0004-6361/202039086

Simon, J. B., Beckwith, K., & Armitage, P. J. 2012, MNRAS, 422, 2685, doi: 10.1111/j.1365-2966.2012.20835.x

Stewart, G. R., & Ida, S. 2000, Icarus, 143, 28, doi: 10.1006/icar.1999.6242

van der Walt, S., Colbert, S. C., & Varoquaux, G. 2011, Computing in Science and Engineering, 13, 22, doi: 10.1109/MCSE.2011.37

Wallace, S. C., & Quinn, T. R. 2019, MNRAS, 489, 2159, doi: 10.1093/mnras/stz2284

Weidenschilling, S. J. 1977, MNRAS, 180, 57, doi: 10.1093/mnras/180.2.57

—. 1989, Icarus, 80, 179, doi: 10.1016/0019-1035(89)90166-8

Wes McKinney. 2010, in Proceedings of the 9th Python in Science Conference, ed. Stéfan van der Walt & Jarrod Millman, 56 – 61

Wetherill, G. W., & Stewart, G. R. 1989, Icarus, 77, 330, doi: 10.1016/0019-1035(89)90093-6

—. 1993, Icarus, 106, 190, doi: 10.1006/icar.1993.1166